The Astrophysical Journal, 931:17 (24pp), 2022 May 20 https://doi.org/10.3847/1538-4357/ac64a3
© 2022. The Author(s). Published by the American Astronomical Society.
OPEN ACCESS

The Redshift Evolution of the Binary Black Hole Merger Rate: A Weighty Matter

L. A. C. van Son[1,2,3], S. E. de Mink[3,1,2], T. Callister[4], S. Justham[2,5,3], M. Renzo[4,6], T. Wagg[7,1,3], F. S. Broekgaarden[1], F. Kummer[2], R. Pakmor[3], and I. Mandel[8,9,10]
[1] Center for Astrophysics | Harvard & Smithsonian, 60 Garden St., Cambridge, MA 02138, USA; lieke.van.son@cfa.harvard.edu
[2] Anton Pannekoek Institute for Astronomy, University of Amsterdam, Science Park 904, 1098XH Amsterdam, The Netherlands
[3] Max Planck Institute for Astrophysics, Karl-Schwarzschild-Str. 1, D-85748 Garching, Germany
[4] Center for Computational Astrophysics, Flatiron Institute, 162 Fifth Avenue, New York, NY 10010, USA
[5] School of Astronomy and Space Science, University of the Chinese Academy of Sciences, Beijing 100012, People's Republic of China
[6] Department of Physics, Columbia University, New York, NY 10027, USA
[7] Department of Astronomy, University of Washington, Seattle, WA, 98195, USA
[8] Monash Centre for Astrophysics, School of Physics and Astronomy, Monash University, Clayton, Victoria 3800, Australia
[9] The ARC Center of Excellence for Gravitational Wave Discovery—OzGrav, Hawthorn VIC 3122, Australia
[10] Birmingham Institute for Gravitational Wave Astronomy and School of Physics and Astronomy, University of Birmingham, Birmingham, B15 2TT, UK
Received 2021 October 2; revised 2022 March 17; accepted 2022 April 4; published 2022 May 19

Abstract

Gravitational-wave detectors are starting to reveal the redshift evolution of the binary black hole (BBH) merger rate, $R_{\rm BBH}(z)$. We make predictions for $R_{\rm BBH}(z)$ as a function of black hole mass for systems originating from isolated binaries. To this end, we investigate correlations between the delay time and black hole mass by means of the suite of binary population synthesis simulations, COMPAS. We distinguish two channels: the common envelope (CE), and the stable Roche-lobe overflow (RLOF) channel, characterized by whether the system has experienced a common envelope or not. We find that the CE channel preferentially produces BHs with masses below about 30 $M_\odot$ and short delay times ($t_{\rm delay} \lesssim 1$ Gyr), while the stable RLOF channel primarily forms systems with BH masses above 30 $M_\odot$ and long delay times ($t_{\rm delay} \gtrsim 1$ Gyr). We provide a new fit for the metallicity-dependent specific star formation rate density based on the Illustris TNG simulations, and use this to convert the delay time distributions into a prediction of $R_{\rm BBH}(z)$. This leads to a distinct redshift evolution of $R_{\rm BBH}(z)$ for high and low primary BH masses. We furthermore find that, at high redshift, $R_{\rm BBH}(z)$ is dominated by the CE channel, while at low redshift, it contains a large contribution (∼40%) from the stable RLOF channel. Our results predict that, for increasing redshifts, BBHs with component masses above 30 $M_\odot$ will become increasingly scarce relative to less massive BBH systems. Evidence of this distinct evolution of $R_{\rm BBH}(z)$ for different BH masses can be tested with future detectors.

Unified Astronomy Thesaurus concepts: Stellar mass black holes (1611); Gravitational wave sources (677); Close binary stars (254); Stellar evolution (1599); Astrophysical black holes (98)

1. Introduction

The Advanced LIGO (LIGO Scientific Collaboration et al. 2015), Advanced Virgo (Acernese et al. 2015), and KAGRA (Akutsu et al. 2021) gravitational-wave detectors are revealing gravitational-wave events that probe a progressively larger fraction of the universe (Abbott et al. 2019a, 2021a, 2021f, 2021g). As the number of gravitational-wave detections increases, they unveil the evolution of the binary black hole (BBH) merger rate with redshift. Current gravitational-wave detectors already probe black holes (BHs) with component masses of about 30 $M_\odot$ out to redshifts $z \sim 1$ (Fishbach et al. 2018; Callister et al. 2020; Abbott et al. 2021a, 2021b, 2021c). Third-generation detectors, scheduled to start observations in the 2030s, promise to observe stellar-mass BBH mergers with component masses in the range ∼5–350 $M_\odot$ out to $z > 10$ (e.g., Sathyaprakash et al. 2019a, 2019b; Maggiore et al. 2020). This means that we are rapidly moving toward a complete picture of both the redshift evolution of the stellar-mass BBHs merger rate and the redshift evolution of source property distributions.

Original content from this work may be used under the terms of the Creative Commons Attribution 4.0 licence. Any further distribution of this work must maintain attribution to the author(s) and the title of the work, journal citation and DOI.

The redshift evolution of the BBH merger rate contains information on the origin of these BBHs; however, a direct interpretation is complicated. To infer the birth time and environment of the observed merging BBHs, we first need to understand the difference between the time at which the progenitor stars formed and the time of merger of the BBH. This is what we define as the delay time $t_{\rm delay}$. It is the sum of two independent timescales: (I) the lifetime of the binary stars up to the moment that both have become compact objects, and (II) the inspiral time of the two BHs up to the BBH merger event. The former timescale, i.e., the lifetime of massive stars, is typically a few Myr. The latter timescale depends primarily on the separation between the two BHs at BBH formation (Peters 1964). To interpret the BBH merger rate, we first need to understand the impact of the delay time distribution on the observed rate at each redshift.

The delay time of BBHs from isolated binaries of interest can range from Myr to more than a Hubble time (see, e.g., Giacobbo & Mapelli 2018; Neijssel et al. 2019). This implies that BBH mergers observed to merge at a given redshift, $z_{\rm merge}$, formed Myr to Gyr earlier. Hence, these mergers are comprised of a mixture of systems that originate from different formation redshifts, and likely probe a range of different formation environments.

The delay time is thus a very important quantity, which, unfortunately, cannot be observed directly for an individual system. It is possible to make statistical inferences about the delay

time distribution using the detections available so far (see, e.g., Fishbach & Kalogera 2021). However, inference of the time-delay distribution is difficult because it is degenerate with the progenitor formation rate. Moreover, we are currently still limited by the low number of sources that are detected out to higher redshifts.

Although the delay time is not directly observable, we will observe the redshift evolution of the source properties, i.e., the BH mass, spin, and mass ratio distributions at different redshifts. Several earlier studies have investigated the evolution of the BBH merger rate with redshift for the total population of merging BBHs (e.g., Rodriguez & Loeb 2018; Mapelli & Giacobbo 2018; Choksi et al. 2019; Santoliquido et al. 2021). The redshift evolution of source property distributions remains relatively obscured, though it is actively being studied (see, e.g., Neijssel et al. 2019; Mapelli 2021). Recent work has hinted toward relations between source properties and redshift evolution. Mapelli et al. (2019), for example, find that massive BBHs tend to have longer delay times in their models. Therefore, an important step to move forward is to associate possible trends in delay time distribution to observable characteristics, while understanding their physical origin.

Here, we inspect the delay time–mass relation for BHs coming from isolated binaries, as predicted by the rapid population synthesis code COMPAS. We consider two main channels: (1) the common envelope channel (or CE channel; see, e.g., Belczynski et al. 2007; Postnov & Yungelson 2014; Belczynski et al. 2016; Vigna-Gómez et al. 2018), including BBH systems where the progenitor system has experienced at least one common envelope, and (2) the stable Roche-lobe overflow channel (or stable RLOF channel; see, e.g., van den Heuvel et al. 2017; Inayoshi et al. 2017). The stable RLOF channel contains all BBH systems that experience *only* stable mass transfer (i.e., all systems that *do not* experience CE events, and so it is the complement set of the CE channel). See also Figure 1 for a cartoon depiction of the most common evolution of these two channels. Note that this does not display all possible variations of the CE and stable RLOF channel. However, other subchannels are rare. For example, the subchannel where both the first and second mass transfer are unstable (which is one of the most common subchannels) contributes only 0.6% to the total rate of BBH mergers as observed by a perfect detector (Equation (6)). The respective contributions of the CE and the stable RLOF channel to the observed population of merging double compact objects is an active area of research (see, e.g., Neijssel et al. 2019; Bavera et al. 2021; Marchant et al. 2021; Gallegos-Garcia et al. 2021). In this work, we aim to use characteristic delay time–mass distributions from each channel to make predictions for observables in the gravitational-wave distributions.

This paper is structured as follows: in Section 2, we describe the population synthesis code COMPAS used in this work. We find that massive BHs ($M_{\rm BH,1} > 30\,M_\odot$, where we define $M_{\rm BH,1}$ as the more massive BH at BBH merger) predominantly form in BBHs with long delay times ($t_{\rm delay} > 1$ Gyr). We show that this can be explained by differences between the CE channel and the stable RLOF channel in Section 3. In Section 4, we describe how we calculate cosmic BBH merger rates. We then discuss how the distinct delay times and mass distributions arising from CE and stable RLOF affect the observed merger rate evolution of BBHs in Section 5. In Section 6, we discuss the prospect of observing trends in the BBH merger rate with current and near-future gravitational-wave detectors. Specifically, our models predict that the slope of the intrinsic BBH merger rate density with redshift is more shallow and starts decreasing at lower redshift for higher $M_{\rm BH,1}$. We discuss the robustness of our main findings and caveats that apply to a population synthesis approach in Section 7, and we summarize our main results in Section 8.

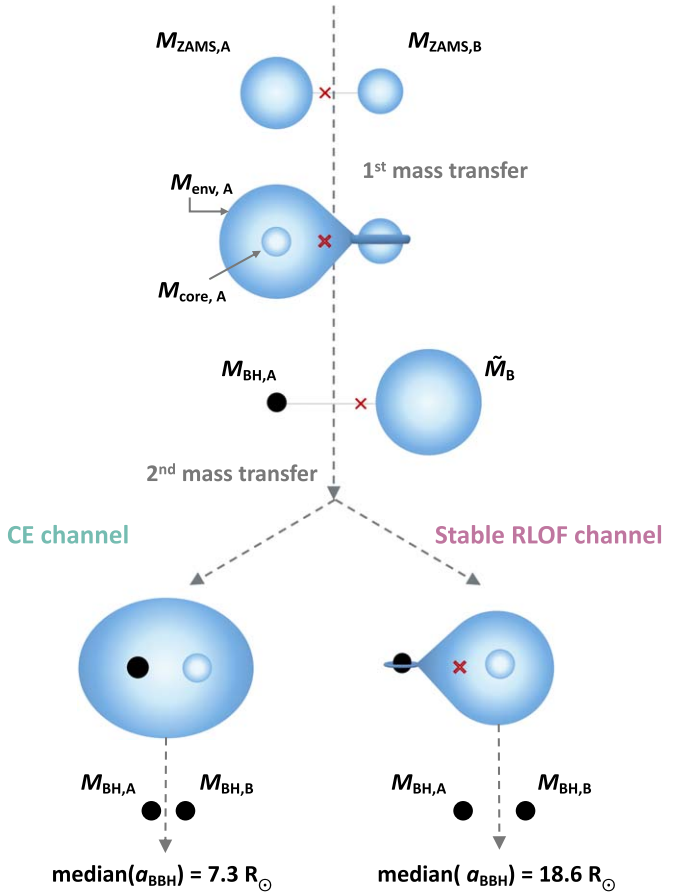

Figure 1. Cartoon depiction of the *typical* evolution of a BBH progenitor system through the stable RLOF and CE channel. Annotations refer to masses at zero-age main sequence ($M_{\rm ZAMS}$), the envelope mass ($M_{\rm env}$), the core mass ($M_{\rm core}$), mass after mass transfer ($\tilde{M}_{\rm B}$), and BH mass ($M_{\rm BH}$). The subscript A (B) denotes the initially more (less) massive star. The red cross gives an impression of the location of the center of mass at the onset of the evolutionary phase depicted (not to scale). The median separation at BBH formation is annotated for each channel, considering BBH mergers that can be observed by a "perfect detector" (see text).

2. Method (I) : Simulating Merging BBH Populations

To simulate the evolution of isolated massive binary star progenitors that lead to merging BBH, we use the rapid population synthesis code that is part of the COMPAS suite[11] (version v02.19.04; see Riley et al. 2022; Stevenson et al. 2017; Vigna-Gómez et al. 2018). We simulate a total of 10^7 binaries. To check that our results are converged, we have repeated all analyses for an independent set of 10^6 binaries, and we found no significant differences. In this section, we discuss the treatment of stellar evolution and binary interaction processes (Section 2.1) and sampling of the initial parameters (Section 2.2).

2.1. Binary Evolution

We model the evolution of massive stars in binary systems using fast algorithms following Hurley et al. (2000, 2002),

[11] See also https://compas.science/.

based on detailed evolutionary models by Pols et al. (1998). Here, we summarize the treatment of the physical processes that are most relevant for this study. For a full description of the code, we direct the interested reader to the references mentioned above.

Winds–For hot O- and B-type stars (with effective temperatures $T_{\rm eff} \geqslant 12,500$ K), we follow Vink et al. (2000, 2001) to account for metallicity-dependent stellar wind mass loss. For cooler, more evolved stars ($T_{\rm eff} \leqslant 12500$K), the mass-loss prescription from Kudritzki & Reimers (1978) and the prescription from Nieuwenhuijzen & de Jager (1990), modified by a metallicity-dependent factor from Kudritzki et al. (1989), are compared and the maximum is adopted. The latter mass-loss prescription is only assumed to be nonzero for stars with luminosity $L > 4000\ L_{\odot}$. For low-mass stars that evolve toward the asymptotic giant branch, the prescription from Vassiliadis & Wood (1993) is added to this comparison. For hot Wolf–Rayet-like stars, we use the empirical mass-loss prescription from Belczynski et al. (2010) that is adapted from Hamann & Koesterke (1998) but scaled by metallicity following Vink & de Koter (2005). For very luminous stars that lie above the Humphreys–Davidson limit, i.e., if the luminosities L and stellar radii R fulfill the condition $L > 6 \times 10^5\ L_{\odot}$ and $(R/\ R_{\odot})(L/\ L_{\odot})^{1/2} > 10^5$ (Humphreys & Davidson 1979), we assume enhanced mass-loss rates following Hurley et al. (2000), motivated by the scarcity of observed stars in this regime and the observed Luminous Blue Variables (LBV) phenomenon. This additional mass loss is metallicity-independent (in line with recent results from, e.g., Davies & Beasor 2020), and is meant to mimic eruptive mass loss.

Stable mass transfer and common envelope phases—We account for mass transfer when a star overflows its Roche lobe (Eggleton 1983). To determine whether Roche-lobe overflow is stable, we use an estimate for the response of the radius of the donor star, R, and its Roche lobe, $R_{\rm RL}$, as a result of mass transfer. COMPAS determines stability by comparing estimates of the adiabatic response of the donor's radius and the response of the donor's Roche-lobe radius (see, e.g., Vigna-Gómez et al. 2018, 2020, and references therein). This procedure depends crucially on the assumed value of $\zeta_* \equiv (\partial \log R/\partial \log M)_{\rm ad}$, with R and M being the radius and mass of the donor star, for different types of donor stars (e.g., Soberman et al. 1997). We assume $\zeta_{\rm ad} = 2$ for main-sequence donors and $\zeta_{\rm ad} = 6.5$ for Hertzsprung-gap donor stars (Ge et al. 2015), and we follow Soberman et al. (1997) for donor stars post-helium ignition.

During stable mass transfer onto a stellar companion, we assume that the accretion rate is limited to 10 times the thermal rate of the accreting star (Neo et al. 1977; Hurley et al. 2002). If the accreting component is a BH, the accretion is assumed to be Eddington-limited. Material lost from the system during nonconservative mass transfer is assumed to carry away the specific orbital angular momentum of the accreting component (e.g., Soberman et al. 1997; van den Heuvel et al. 2017). This reduces the orbital angular momentum and can lead to either shrinking or widening of the orbit, depending on the fraction of mass that is accreted and the binary's mass ratio (e.g., van Son et al. 2020, Appendix A).

Unstable mass transfer is assumed to result in CE evolution (Paczynski 1976; Ivanova et al. 2013, 2020). We assume that ejecting the envelope shrinks the binary orbit following the energy considerations proposed by Webbink (1984) and de Kool (1990). Here, the pre-CE binding energy of the donor's envelope is equated to the orbital energy that becomes available by shrinking the orbit. How efficiently this orbital energy can be used to eject the envelope is parameterized by the $\alpha_{\rm CE}$ parameter, which is set to one in this work. For the binding (and internal) energy of the envelope, we use the "Nanjing" prescription (Dominik et al. 2012), based on fits provided by Xu & Li (2010a, 2010b). We adopt the *pessimistic* CE scenario from Dominik et al. (2012), that is, we assume that Hertzsprung Gap donor stars do not survive a CE event.

Supernovae, kicks, and compact remnants—To model natal supernova kicks, we draw kick velocities with random isotropic orientations and draw the kick magnitudes from a Maxwellian distribution (Hobbs et al. 2005). BH kicks are reduced by the amount of mass falling back onto the newly formed BH during the explosion mechanism, following the "delayed" prescription from (Fryer et al. 2012). This prescription assumes full fallback for BHs resulting from progenitors with a carbon–oxygen core mass $M_{\rm CO} > 11\ M_{\odot}$, and hence these BHs receive no supernova kick.

The remnant mass is modeled as a function of the estimated $M_{\rm CO}$ at the moment of core collapse following Fryer et al. (2012). Stars with helium cores above 35 $M_{\odot}$ at the moment of core collapse are assumed to experience pulsational pair instability following Farmer et al. (2019). Stars with helium core masses between 60 and 135 $M_{\odot}$ at the moment of core collapse are expected to be completely disrupted by pair instability, and therefore leave no remnant BH. With this implementation, the lower edge of the pair-instability mass gap is located at about 45 $M_{\odot}$ (Stevenson et al. 2017; Marchant et al. 2019; Farmer et al. 2019, 2020; Woosley & Heger 2021, but see, e.g., Mehta et al. 2022). Due to the metallicity dependence of stellar winds and the adopted pulsational pair-instability prescription, the maximum BH mass is also metallicity-dependent. The upper limit of about $45\ M_{\odot}$ is only reached for the lowest-metallicity systems (with $Z \lesssim 0.001$). For reference, systems with metallicities of about $Z \sim 0.01$ and $Z \sim 0.0032$ can maximally achieve respective BH masses of about $18\ M_{\odot}$ and $32\ M_{\odot}$ in our simulations (see Figure 7 for a decomposition of the BH mass distribution by metallicity).

2.2. Sampling

The evolution of a binary system is mainly a function of its initial metallicity Z, initial primary and secondary mass M_1 and M_2, and the initial separation a.

We sample birth metallicities with a probability distribution that is flat-in-log in the range $10^{-4} \leqslant Z \leqslant 0.03$. Sampling metallicities from a smooth probability distribution is an improvement over discrete sets of metallicity, which is the most common technique in binary population synthesis studies (but see, for example, Riley et al. 2021, for an exception). Smoothly sampling birth metallicity avoids artificial peaks in the BH mass distribution (e.g., Dominik et al. 2015; Kummer 2020). The flat-in-log distribution ensures that we sample ample binaries at the low metallicities that are favored for BBH formation. Later in this paper, when we calculate cosmic merger rates, we reweight systems to account for the metallicity-dependent star formation (see Section 4). We adjust the normalization of this reweighting over the metallicity range of our simulations, to preserve the correct total star formation rate, i.e., star formation at more extreme metallicities is not discarded.

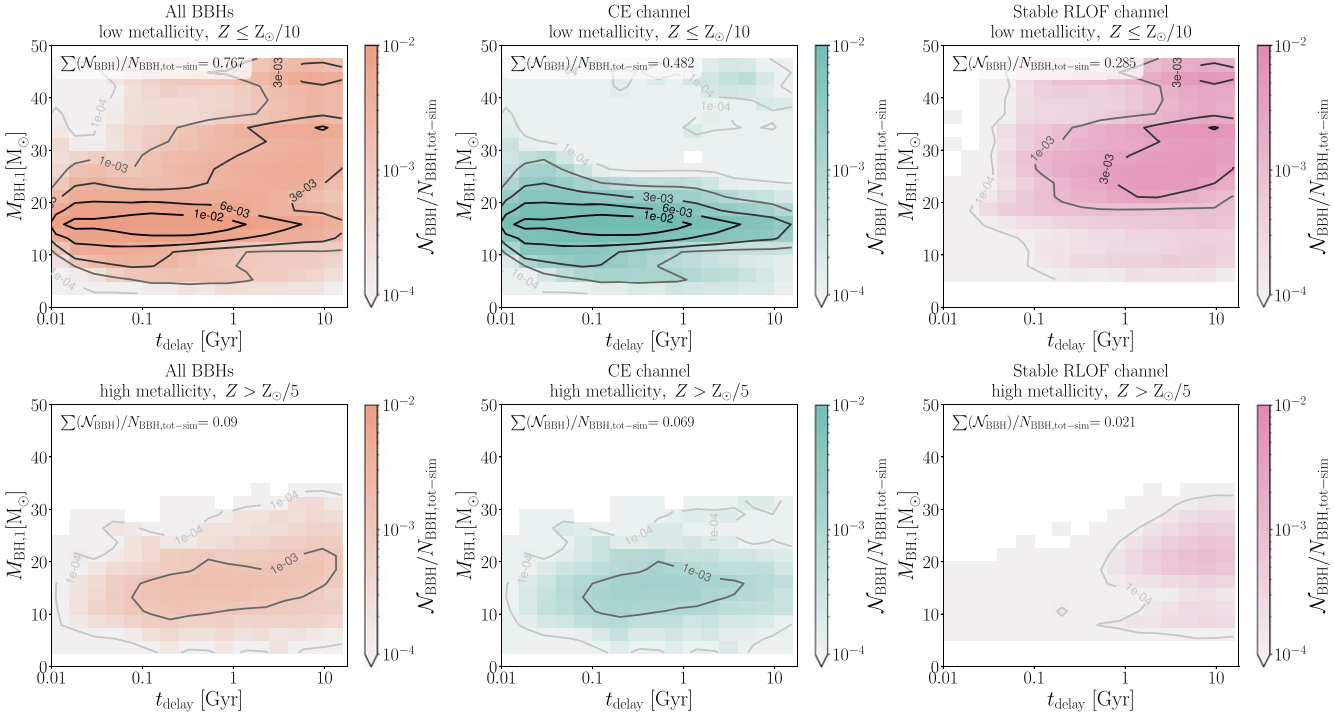

Figure 2. Two-dimensional histograms of the distribution of delay times and primary masses for BBHs in our simulation. The top and bottom rows show results for low ($\leqslant Z_\odot/10$) and high ($> Z_\odot/5$) metallicity, respectively. The leftmost panels show all BBHs, while the middle and rightmost panels are split by formation channel. All histograms are normalized relative to the total simulation including all simulated metallicities. The color bar and contours thus indicate the relative frequency of occurrence in our simulations. We use bin sizes of $\Delta \log_{10}(t_{\rm delay}) = 0.2$ and $\Delta M_{\rm BH,1} = 2.5\ M_\odot$. All panels reveal a lack of BBH systems with high mass ($M_{\rm BH,1} \gtrsim 30\ M_\odot$) and short delay time ($t_{\rm delay} \lesssim 0.1$ Gyr).

We assume the masses of the initially more massive stellar components (the primary, M_1) are universally distributed following a Kroupa (2001) initial mass function and draw masses in the range 10–150 $M_\odot$, in order to focus on stars that evolve into BHs. The binary systems are assumed to follow a uniform distribution of mass ratios ($0.01 \lesssim q \equiv M_2/M_1 < 1.0$, with M_2 being the mass of the secondary star). We require $M_2 \geqslant 0.1\ M_\odot$. The initial binary separations are assumed to follow a distribution of orbital separations that is flat in the logarithm (Öpik 1924) in the range 0.01–1000au. Binary systems that fill their Roche lobe at zero-age main sequence (ZAMS) are discarded. All binary orbits are assumed to be circular at birth.

If a ZAMS star is rotating faster than the metallicity-dependent rotational frequency threshold described in Riley et al. (2021), the binary is assumed to evolve chemically homogeneously. In this work, we focus on the "classical" pathway of isolated binaries toward merging BBHs, and thus we exclude chemically homogeneously evolving stars from our sample.

Because BBH mergers are intrinsically very rare events, direct sampling of the birth distributions is very inefficient and time-consuming. We therefore make use of the adaptive importance sampling code STROOPWAFEL. This algorithm consists of an initial exploration phase to find regions of interest in the binary parameter space. In a subsequent adaptive refinement phase, we optimize the simulations by sampling near the regions of interest (see Broekgaarden et al. 2019, for details).

3. BH Mass–Delay Time Relations

In this section, we first explore the types of BBHs that can be produced by the isolated channel, according to our simulations. We aim to find links between the delay time $t_{\rm delay}$ and observable properties, such as BH masses and spins. Of these, the BH mass is observationally the best-constrained source property. Hence, our main focus is on the BH mass. While we do not discuss BH spins here, previous studies have argued that tidal spin-up is most likely in close binaries with short delay times (e.g., Kushnir et al. 2016; Zaldarriaga et al. 2018; Bavera et al. 2020). In Appendix A, we additionally investigate the correlations between BBH mass ratios and $t_{\rm delay}$.

In Figure 2, we show two-dimensional histograms of $t_{\rm delay}$, and the mass of the heavier BH, $M_{\rm BH,1}$, for BBHs in our simulations. In the top row, we show results for low metallicity, which is representative for the majority of BBH formation (defined as $Z \leqslant Z_\odot/10$, with solar metallicity $Z_\odot = 0.014$; see Asplund et al. 2009). To elucidate the impact of metallicity, we show results for the highest metallicities ($Z > Z_\odot/5$) in the bottom row. In the left column, we show the results for all BBHs in the selected metallicity range. In the middle and right columns, we show the separate contributions of the CE and stable RLOF channel, respectively. All histograms shown are normalized relative to the number of merging BBHs in our full simulation, combining all metallicities. The color shading and contours thus indicate the relative frequency with which these combinations of primary mass and delay time occur in our full set of simulations. We refer the reader to Section 2 for details on how the progenitors are sampled and weighed in our simulation. We note that the underlying distribution in metallicity that is implicitly assumed here is not representative for star formation in the universe. Nevertheless, these diagrams are useful to understand trends in the delay times and primary BH masses at low and high metallicity.

When inspecting the leftmost panel in the top row of Figure 2, which shows the results for all BBH in our simulations for low metallicity, we observe two main components. First, we see that the histogram peaks at delay times of ∼0.1–1 Gyr and primary BH masses of ∼18 $M_\odot$. This peak comes predominantly from systems formed through the CE channel (as can be seen from the top middle panel). Second, we see a noticeable tail of more massive systems $M_{\rm BH} \gtrsim 20\,M_\odot$ with longer delay times around ∼10 Gyr, which predominantly come from the stable RLOF channel (as can be seen in the top rightmost panel). Finally, we see a dearth of BBH systems with high masses ($M_{\rm BH,1} \geqslant 30\,M_\odot$) and short delay times ($t_{\rm delay} \leqslant 0.1$ Gyr), which are not formed by either of the channels considered here.

Comparing low and high metallicity (top and bottom row, respectively), we see that the same two components are present, but the systems with highest mass are absent at high metallicity. This result can be understood as the effect of the metallicity-dependent stellar winds, which are stronger for higher metallicity (e.g., Vink & de Koter 2005). The high-metallicity systems thus also display a lack of BH systems with high masses ($M_{\rm BH,1} \geqslant 30\,M_\odot$) and short delay times ($t_{\rm delay} \leqslant 0.1$ Gyr).

In the following subsections, we discuss the origin for these features.

3.1. Why the CE Channel Does Not Produce High-mass Black Holes

We find that the massive progenitor stars that lead to BHs with masses $M_{\rm BH,1} > 30\,M_\odot$ are disfavored from engaging in —and surviving—CE events in our simulations, because of a variety of effects. To form such BHs, we need stars that form helium cores of at least $M_{\rm He} \gtrsim 30\,M_\odot$. Such cores can only be formed in the most massive stars in our simulations, typically with zero-age main-sequence masses of 60 $M_\odot$ and higher, although we note that the exact value is quite uncertain. Such massive stars are unlikely to engage in and survive a CE, for several reasons.

First of all, the massive progenitors of heavy black holes are thought to experience heavy mass loss, which can remove a large part of the hydrogen envelope before the stars initiates interaction with its companion. Although mass loss by radiatively driven winds is thought to be reduced at low metallicity, mass loss via LBV eruptions is likely to still be very significant also at low metallicity (e.g., Smith 2014; Sanyal et al. 2017; Kalari et al. 2018; Davies et al. 2018; Higgins & Vink 2020; Sabhahit et al. 2021; Gilkis et al. 2021). In fact, such heavy mass loss can prevent massive stars in wider binaries from ever filling their Roche lobe (Mennekens & Vanbeveren 2014; Belczynski et al. 2016). In our simulations, this is the dominant reason for the suppression of the CE channel at higher masses.

Second, even if a massive progenitor were to fill its Roche lobe, it is unlikely to do so while it has a convective envelope. It is generally thought that donor stars with extended convective envelopes are favored for successful ejection of a common envelope. This is mainly because convective stars have large dimensions, and a relatively large fraction of the mass is located at large radii. The binding energy of the envelopes of such stars is thus low with respect to radiative counterparts, and it is thought that the envelope can therefore more easily be removed by an inspiraling companion, as recently emphasized by Klencki et al. (2021) and Marchant et al. (2021). Very massive stars typically do not grow to the dimensions needed to cool their envelope sufficiently to become unstable against convection. Even though some massive stars may manage to develop a deep convective envelope, they do not significantly expand further in radius (in contrast to less massive stars that will ascend the giant branch). Hence, very massive stars generally fill their Roche lobe at an earlier point in their evolution, when the envelope is still radiative. Overall, the occurrence of successful CE is therefore very rare for such massive stars.

Third, and closely related to the second effect, mass transfer from high-mass donor stars is preferentially stable and hence it does not initiate a CE phase. This is especially true for radiative donors, as the early adiabatic response of radiative envelopes to mass loss is contraction (see, e.g., Hjellming & Webbink 1987). Recent studies, based on simulations with a more sophisticated treatment of the physics, tend to emphasize this finding for convective donors as well (e.g., Pavlovskii & Ivanova 2015; Pavlovskii et al. 2017; Marchant et al. 2021). In addition, albeit more speculatively, this effect may be enhanced by the role of envelope inflation. This occurs in massive stars that are close to the Eddington limit. They can develop extended halos (e.g., Sanyal et al. 2015; Jiang et al. 2015, 2018). This can likely cause stable mass exchange before the star has really filled its Roche lobe. Although our simulations treat the stability criteria in a very simplified way, the recent studies mentioned above tend to strengthen our findings that mergers involving more massive BHs are unlikely from the CE channel.

We remind the reader that, in the CE channel, it is normally the second phase of mass transfer where the common envelope phase occurs; see Figure 1. The considerations above thus primarily concern the initially less massive star in the binary system. In principle, it is possible to form BBH mergers with at least one heavy BH from binary systems with a very massive primary ($\gtrsim$60 $M_\odot$) and a significantly less massive secondary ($\lesssim$40 $M_\odot$). The heavy BH then originates from the primary star, while the secondary star is of low enough mass to initiate a CE phase in which the envelope is ejected successfully. However, we find that such systems are extremely rare. The secondary typically accretes during the first mass-transfer phase and becomes massive enough to be subject to the first two effects mentioned above. This scenario thus only works for systems with extreme initial mass ratios. Such systems tend to merge upon the first mass transfer phase and will thus not be able to form BBHs that merge within a Hubble time.

Overall, we find that the formation of BBHs with at least one heavy BH is not impossible through the CE channel, but it is very unlikely in our simulations. More detailed recent studies on partial aspects of the problem strengthen this finding.

3.2. Why the Stable RLOF Channel Does Not Produce Short Delay Times

We find that the stable RLOF channel leads to longer delay times than the CE channel, due to longer inspiral times. These longer inspiral times are caused by wider separations (larger semimajor axis) at BBH formation. We find that the median separation at BBH formation is about $7\,R_\odot$ for systems that came from the CE channel, and about $20\,R_\odot$ for systems that come from the stable RLOF channel, when considering all systems that can be observed by a "perfect detector" (see Equation (6)). Wider separations lead to longer inspiral times because the orbital decay time from gravitational-wave

emission scales with the fourth power of the separation (Peters 1964). We find that the effects of the component masses and eccentricities of BBH systems are typically subdominant to the effect of the separation.

To understand why the CE channel produces shorter separations, we consider the difference in orbital evolution for both channels. For stable mass transfer, whether the orbit widens or shrinks depends on the mass ratio, the amount of mass lost from the system, and the assumed angular momentum that is carried away by the mass that is lost (e.g., Soberman et al. 1997). To produce merging BBH systems through stable RLOF, we typically need to considerably shrink the orbit during reverse mass transfer (van den Heuvel et al. 2017). The accretor is already a BH at this time, and its accretion is assumed to be limited to the Eddington accretion rate. This means that most of the mass that is transferred is lost from the system. For highly nonconservative mass transfer, the orbit shrinks (when $M_{\rm acc}/M_{\rm donor} \leqslant 0.79$; for which case, see, e.g., Appendix A from van Son et al. 2020) under the assumption that mass is lost from the vicinity of the accreting companion and has the specific angular momentum of the accretor's orbit. This criterion may be fulfilled when the secondary star fills its Roche lobe at first and lead to shrinking of the orbit, but as more mass is lost, the orbital evolution can reverse from shrinking to widening. In contrast, CE evolution exclusively shrinks the orbit in our simulations, in agreement with general expectation (e.g., Paczynski 1976; Ivanova et al. 2013).

Even though many of the details regarding orbital shrinking are uncertain in both scenarios, these mechanisms are so different that we can robustly expect substantial differences in the resulting final separations. Since the separation is the dominant term in the expression for the inspiral time, we are confident that our finding that the two channels lead to a difference in their delay times is robust, at least qualitatively. For completeness, we show the delay times' distributions, which are similar to those in Figure 2, but for all metallicities and integrated over $M_{\rm BH,1}$ in Appendix B.

4. Method (II) : Calculating Intrinsic Merger Rates

To place our results into cosmological context, we need to integrate over the metallicity-dependent star formation rate density, $\mathcal{S}(Z, z)$ (see also Dominik et al. 2013, 2015; Belczynski et al. 2016; Mandel & de Mink 2016; Chruślińska et al. 2018). This results in an intrinsic BBH merger rate density, $R_{\rm BBH}(z)$, that we will discuss in Sections 5.1 and 6. Throughout this work, we adopt cosmological parameters consistent with the WMAP9–cosmology (Hinshaw et al. 2013) including $h = {\rm H}_0\ /(100\ {\rm km\ s^{-1}\ Mpc^{-1}}) = 0.693$, where H_0 is the Hubble constant.

4.1. Estimating the Intrinsic BBH Merger Rate

We follow the method described in Neijssel et al. (2019) and Broekgaarden et al. (2021a) to calculate the BBH merger rate.[12] The number of detections that occur during the active observing time ($T_{\rm obs}$, measured in the detector frame at $z = 0$) of an infinitely sensitive gravitational-wave detector is given by

$$\frac{d^2N_{\rm det}}{d\zeta dz} = \frac{R_{\rm BBH}(z,\,\zeta)}{d\zeta}\left[\frac{dV_c}{dz}(z)\right]\frac{T_{\rm obs}}{1+z}, \tag{1}$$

where $N_{\rm det}$ is the number of detectable BBH mergers, ζ is the set of parameters that describe a BBH, and $\frac{dV_c}{dz}(z)$ is the differential comoving volume per redshift (see, e.g., Abbott et al. 2019b).

Our goal is to estimate the intrinsic merger rate density of all BBHs in the source frame, $R_{\rm BBH}(z)$:

$$R_{\rm BBH}(z) = \int d\zeta\ R_{\rm BBH}(z,\,\zeta) = \frac{d^2N_{\rm BBH}}{dV_c\,dt}(z)\ [{\rm cGpc^{-3}\ yr^{-1}}], \tag{2}$$

which is the number of mergers $N_{\rm BBH}$ per comoving volume V_c in a comoving gigaparsec, ${\rm cGpc^{-3}}$, per year, with t being the time in the source frame.

Often, we would like to evaluate the intrinsic rate density over larger redshift bins. For that purpose, we define the volume averaged intrinsic merger rate density:

$$\overline{R}_{\rm BBH}(z) = \frac{\int_{z_{\rm min}}^{z_{\rm max}} R_{\rm BBH}(z)\frac{dV_c}{dz}\,dz}{\int_{z_{\rm min}}^{z_{\rm max}} \frac{dV_c}{dz}\,dz}\ [{\rm cGpc^{-3}\ yr^{-1}}]. \tag{3}$$

To approximate the intrinsic merger rate density at redshift z, we convolve the number of BBH mergers per unit of star-forming mass with the star formation rate density over the merger time $t_m(z)$, and integrate this over all metallicities:

$$R_{\rm BBH}(z,\,\zeta) = \int dZ' \int_0^{t_{\rm m(z)}} dt'_{\rm delay} \times \underbrace{\frac{d^2N_{\rm form}}{dM_{\rm SF}\ dt_{\rm delay}}(Z',\,t'_{\rm delay},\,\zeta)}_{\text{BBH formation rate}} * \underbrace{\mathcal{S}(Z',\,z(t_{\rm form}))}_{Z-\text{dependent SFRD}}, \tag{4}$$

where the time of merger, $t_m(z)$, delay time, $t_{\rm delay}$, and formation time, $t_{\rm form}$, are related by $t_{\rm form} = t_m - t_{\rm delay}$. We adopt the redshift of first star formation $z_{\rm first\ SF} = 10$ in our work. Equation (4) is evaluated at redshift steps of $dz = 0.001$.

Our choice for the metallicity-dependent star formation rate at the formation redshift, $\mathcal{S}(Z, z_{\rm form}(t_{\rm form}))$, is detailed and discussed in Appendix C. Here, $d^2N_{\rm form}/(dM_{\rm SF}\,dt_{\rm delay})$ is the number of BBH systems that form with delay times in the interval $dt_{\rm delay}$ per unit of star-forming mass $dM_{\rm SF}$. Because we model only a small fraction of the total star-forming mass, we need to renormalize our results, given the initial distributions of primary masses and mass ratios (see Section 2.2). In our simulations, we neglect single stars, only draw primary masses in the range 10–150 $M_\odot$, and apply adaptive importance sampling. When renormalizing, we assume that the universe has a constant binary fraction of $f_{\rm bin} = 0.7$ (Sana et al. 2012) and that stars are formed with initial masses in the range 0.1–200 $M_\odot$.

5. The Merger Rates and Mass Function at Different Redshifts

5.1. The Role of the Two Formation Channels

In Figure 3, we show the averaged intrinsic merger rate density $\overline{R}_{\rm BBH}(z)$, as a function of redshift, z, and per primary BH mass, $M_{\rm BH,1}$. We split the rate by channel, showing the CE and stable RLOF channel in the bottom left and right panels, respectively.

[12] The scripts to compute the rates are available as part of the COMPAS suite https://github.com/TeamCOMPAS/COMPAS.

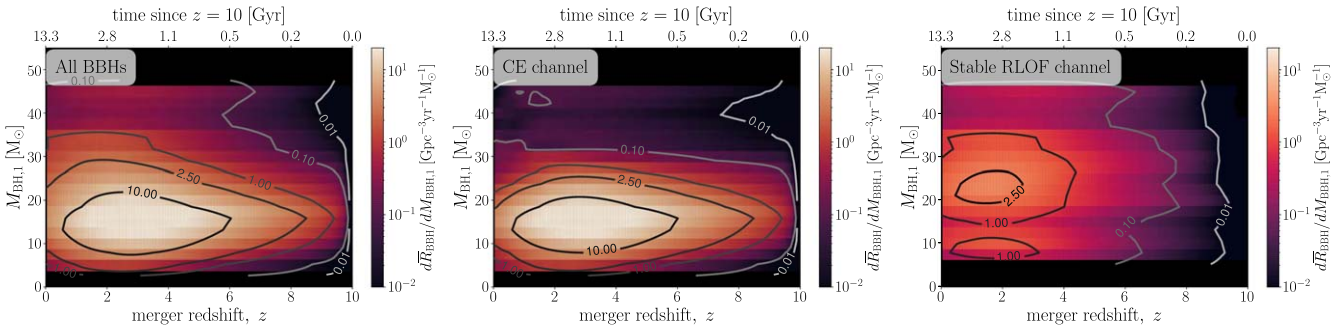

Figure 3. The averaged intrinsic merger rate density $\overline{R}_{\rm BBH}(z)$, for redshift bins of $dz = 0.2$, and primary BH mass bins of $dM_{\rm BH,1} = 2.5\ M_\odot$. The top axis shows the time passed since $z = 10$, which we have chosen as the redshift of first star formation. The left panel shows the full distribution. The middle panel shows mergers of systems that have experienced at least one CE during their evolution, while the right panel shows mergers of systems that formed through the stable RLOF channel. All panels show a dearth of high-mass BHs ($M_{\rm BH,1} \gtrsim 30\ M_\odot$) merging at higher redshifts ($z > 6$).

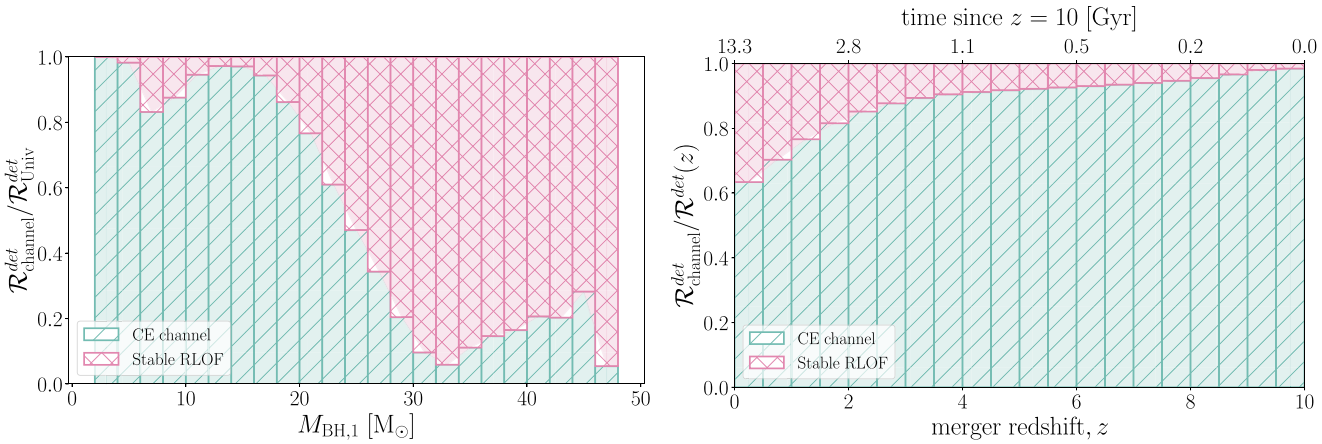

Figure 4. Fractional contribution of the CE channel (green hatched) and the stable RLOF channel (pink cross hatched) to $\mathcal{R}^{\rm det}(z, \zeta)$. Left panel shows the relative contributions to $\mathcal{R}^{\rm det}(z, \zeta)$ per mass bin after integrating over all redshifts. Right panel shows the fractional contribution to $\mathcal{R}^{\rm det}(z, \zeta)$ integrated over all $M_{\rm BH,1}$, as a function of redshift.

In the left-hand panel, we see that the overall BBH merger rate density peaks around redshift 2−3, and at a mass of about 15 $M_\odot$ for the most massive BH. The merger rate decreases toward higher mass and higher redshift. Comparing the middle and right panels, we see that the CE channel and RLOF channel contribute to the rate in distinct ways.

We would like to quantify the relative contribution of each channel to the production of $M_{\rm BH,1}$. For this purpose, we define the total rate of BBH mergers in the detector frame as:

$$\mathcal{R}^{\rm det}(z, \zeta) = \frac{R_{\rm BBH}(z, \zeta)}{1+z}\frac{dV_c}{dz}. \tag{5}$$

Integrating this from redshift zero to the redshift of first star formation, we obtain the total rate of BBH mergers throughout the universe:

$$\mathcal{R}^{\rm det}_{\rm Univ}(\zeta) = \int_0^{z_{\rm first\ SF}} dz\ \mathcal{R}^{\rm det}(z, \zeta). \tag{6}$$

This is the same as the BBH merger rate as observed by an infinitely sensitive detector at redshift zero. In the left-hand panel of Figure 4, we show what fraction of $\mathcal{R}^{\rm det}_{\rm Univ}(\zeta)$ derives from which channel for different values of $M_{\rm BH,1}$. This emphasizes how the stable RLOF channel dominates $\mathcal{R}^{\rm det}_{\rm Univ}(\zeta)$ at higher masses, while the CE channel dominates for primary BH masses below 25 $M_\odot$.

The formation channels differ in how they contribute to the intrinsic merger rate density as a function of redshift. Specifically, the contribution of the stable RLOF channel decreases faster toward higher redshifts than the CE channel. As a result, the CE channel becomes increasingly dominant toward higher redshifts. To show this more clearly, we again integrate $\mathcal{R}^{\rm det}(z, \zeta)$, but now over all $M_{\rm BH,1}$ to obtain $\mathcal{R}^{\rm det}(z)$. We show what fraction of $\mathcal{R}^{\rm det}(z)$ derives from which channel for different redshift bins in the right-hand panel of Figure 4. Overall, the CE channel is dominant, but the stable RLOF channel becomes more important at low redshift, and is responsible for about 40% of BBHs merging in the local universe.

The reduced contribution of the stable RLOF channel at higher redshifts is a result of the scarcity of short delay times in this channel, as shown in Figure 2. Systems coming from the stable RLOF channel generally have delay times $\gtrsim$1 Gyr. At redshift 6, only 0.5 Gyr has passed since our adopted redshift of first star formation ($z = 10$). This means that systems coming from the stable RLOF channel have typically not had enough time to merge at these high redshifts. For completeness, we show the distributions similarly to Figure 3, but for chirp mass $M_{\rm chirp}$, in Appendix D.

In Figure 5, we display the distribution of $M_{\rm BH,1}$ split by formation channel, for merger redshifts between 0 and 0.5 (see Equation (3)). The results in Figure 5 imply that the high-mass merger events that have been detected so far at relatively low

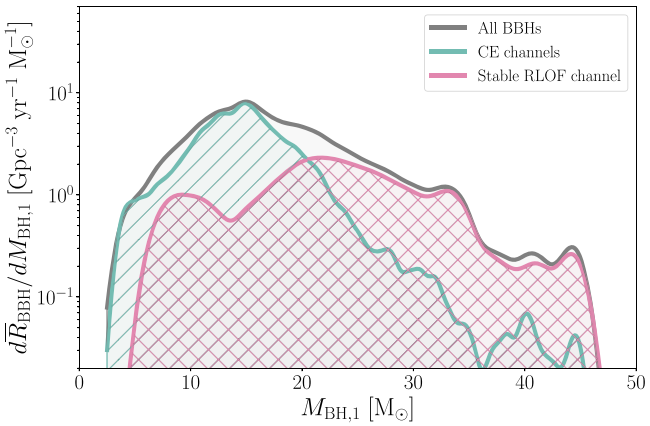

Figure 5. Distribution of primary BH masses $M_{\rm BH,1}$ split by formation channel, for merger redshifts between $0 \leqslant z < 0.5$.

redshift primarily come from the stable RLOF channel (assuming that the observed BBH merger rate is dominated by these two channels). This is in contrast to the results in, e.g., Belczynski et al. (2016) and Stevenson et al. (2017), but agrees with findings in more recent work from, e.g., Neijssel et al. (2019) and Gallegos-Garcia et al. (2021).

5.2. The Shape of the Mass Function at Different Redshifts

In the left panel of Figure 6, we show the $M_{\rm BH,1}$ distribution for different redshift bins (again adopting the averaged intrinsic merger rate density $\overline{R}_{\rm BBH}(z)$ for every redshift bin). We see that there are features of the mass distribution that persist in all redshift bins. First, the peak of the distribution occurs at $\sim$18 $M_\odot$. From Figures 2 and 3, we find that this peak originates from the CE channel.

In every redshift bin, $\overline{R}_{\rm BBH}(z)$ decays for BH masses above $\sim$18 $M_\odot$. In part, the slope on the right side of $\sim$18 $M_\odot$ is steepened due to the decay of the initial mass function toward higher mass stars. However, the primary driver behind the decay toward higher masses is the effect of metallicity: higher metallicities lead to more mass loss through stellar winds, and therefore shift the maximum possible $M_{\rm BH,1}$ to lower values. In Figure 7, we show this shift in the maximum BH mass by dissecting the $M_{\rm BH,1}$ distribution for $0 < z < 0.5$ into bins of different formation metallicities. This shows that the maximum BH mass is about 18 $M_\odot$ in our simulations for the high metallicities ($Z \gtrsim 0.01$) that dominate the metallicity-dependent star formation rate density, $\mathcal{S}(Z, z)$. For completeness, we show the $M_{\rm BH,1}$ distribution split by both formation channel and formation metallicity in appendix Figure 13. This shows that the stable RLOF channel dominates the higher-mass end of the distribution at every metallicity.

The decay of the distribution for BH masses below $\sim$18 $M_\odot$ in Figure 6, can be understood as a combination of our adopted SN kick and CE physics. First, above carbon–oxygen core masses of $M_{\rm CO} = 11\,M_\odot$, BHs are assumed to experience full fallback, and hence receive no kick. BHs from lower-mass progenitors are expected to receive higher SN kicks (given the adopted BH-kick prescription from Fryer et al. 2012). These higher SN kicks can unbind the binary system and thus prevent the formation of a merging BBH system (see also panels M, N, and O in Figure 15). Second, for the same change in orbital separation, lower-mass BHs can provide less orbital energy to help unbind the common envelope. This means that progressively lower-mass BHs will fail to eject their companion's envelope at a given CE efficiency $\alpha_{\rm CE}$. Increasing $\alpha_{\rm CE}$ will allow successful CE ejection for lower-mass BHs, thus pushing the peak of the mass distribution to lower-mass BHs (see also panels F–I Figure 15).

Apart from the peak in Figure 6, two other distinct features persist in all redshift bins. The first is the rise in $R_{\rm BBH}(z)$ just before the edge of the distribution at $M_{\rm BH,1} \approx 45\,M_\odot$. This feature is caused by the prescription for pair pulsations. Specifically, we adopted the prescriptions from Farmer et al. (2019) (see Section 2). This is also called the "pulsational pair-instability supernova" (or PPISN) pileup (e.g., Talbot & Thrane 2018; Marchant et al. 2019). Second, there is a bump at $M_{\rm BH,1} \sim 35\,M_\odot$. This bump is an artifact of the transition between prescriptions for remnant masses from core-collapse supernovae (CCSN, following Fryer et al. 2012) to remnant masses from pair pulsational instability supernovae (from Farmer et al. 2019). Though the bump in our results is an artificial feature, it is not clear whether the transition between core-collapse supernovae and pair pulsational supernovae should be smooth. For example, Renzo et al. (2020b) argue that such a discontinuity can occur if convection is not efficient at carrying away energy for the lowest-mass systems that experience pair pulsations. Furthermore, Abbott et al. (2021b) find evidence for an overdensity in the merger rate (>99% credibility) at $M_{\rm BH,1} = 35^{+1.5}_{-3.1}\,M_\odot$. It is difficult to attribute this observed peak to the PPISN pileup at the lower edge of the PISN mass gap, since stellar models predict this pileup to occur at masses of about 40–60 $M_\odot$ (see, e.g., Marchant et al. 2019; Farmer et al. 2019; Renzo et al. 2020a, 2020b; Marchant & Moriya 2020; Woosley & Heger 2021; Costa et al. 2021, and references therein).

To investigate the redshift evolution of the primary BH mass distribution, in the right panel of Figure 6 we show the intrinsic distribution normalized by the peak rate for each redshift bin. We focus on redshifts in the range $0 < z \leqslant 2$, because a large absolute change in $R_{\rm BBH}(z)$ is contained in this redshift range (see Figure 8), while the contribution from different metallicities to $\mathcal{S}(Z, z)$ does not vary greatly up to $z \sim 1.5$. The right panel of Figure 6 shows that the high-mass end ($M_{\rm BH,1} > 18\,M_\odot$) decays faster at higher redshifts than the low-mass end ($M_{\rm BH,1} \leqslant 18\,M_\odot$) of the distribution. We find that the ratio of $M_{\rm BH,1} > 18\,M_\odot / M_{\rm BH,1} \leqslant 18\,M_\odot$ is about 0.7 in the redshift bin 0–0.5, while it is about 0.45 in the redshift bin 1–1.5. The steeper decay of the high-mass end of the mass distribution for higher redshifts can be explained by the scarcer contribution of the stable RLOF channel (which is responsible for the high-mass end of the mass distribution) toward higher redshifts, as discussed above in Section 5.1.

6. Prospects for Observing Trends with Redshift in the Intrinsic Merger Rate Density

Third-generation detectors promise to probe BBH mergers across all redshifts of interest, but these instruments are still at least a decade away (e.g., Sathyaprakash et al. 2019a). Present-day detectors are, however, already beginning to probe the evolution at low redshift.

In the previous section, we found the evolution of the high-mass slope of the predicted $M_{\rm BH,1}$ distribution for redshifts in the range 0−2. Since current ground-based detectors already detect many systems with $M_{\rm BH,1} > 20\,M_\odot$, it is possible to start

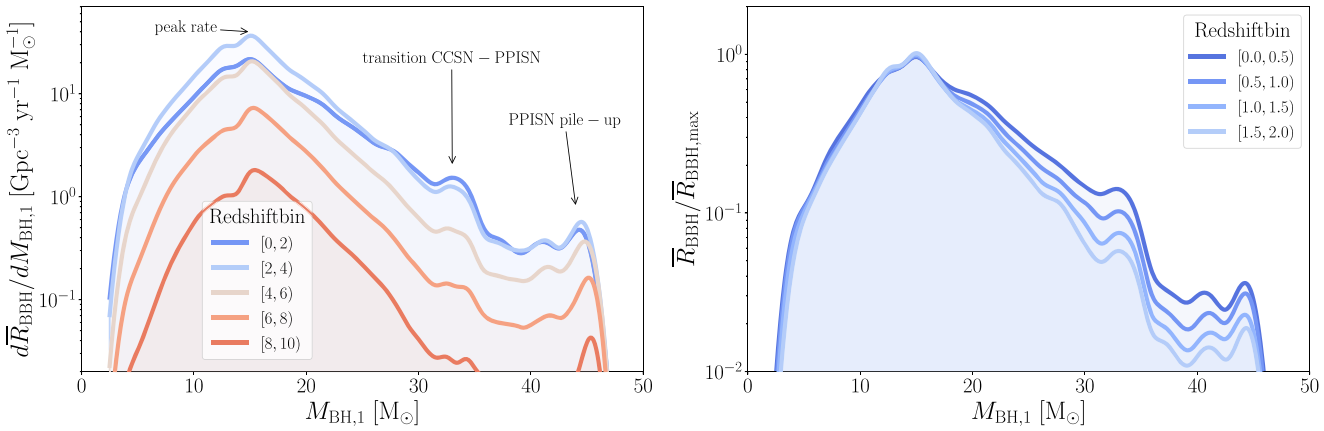

Figure 6. Distribution of primary BH masses $M_{\rm BH,1}$ for several redshift bins. The left panel shows the general trend for different redshift bins. The right panel shows the same distribution normalized by the peak rate value for the given redshift bin, with a focus on redshifts up to $z = 2$. Both distributions are shown down to $M_{\rm BH,1} = 2.5\,M_\odot$, which is our minimum allowed BH mass. This shows that the distribution of primary BH masses evolves with redshift.

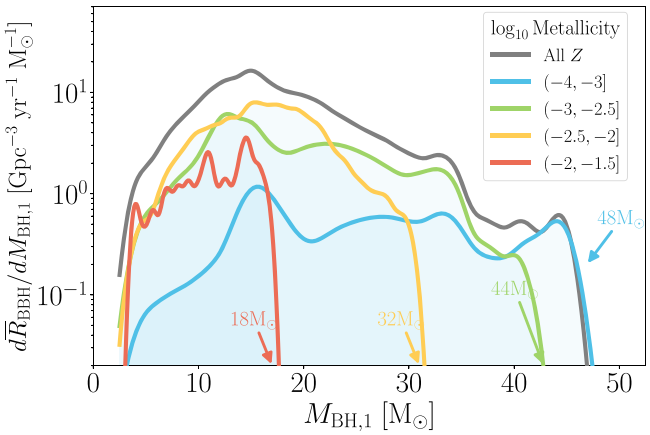

Figure 7. Breakdown of the $M_{\rm BH,1}$ mass distribution by birth metallicity for all BBH mergers between redshifts $0 \leqslant z < 0.5$. The maximum BH mass that contributes to each metallicity bin is annotated.

probing this mass-specific redshift evolution of the merger rate $R_{\rm BBH}(z)$ (Abbott et al. 2021d, 2021b).

In this section, we explore the possibility of probing trends of the rates separated by mass bin as a function of redshift. In Section 6.1, we show our predictions, and in Section 6.2, we discuss whether these effects are observable in the second gravitational-wave transient catalog (GWTC-2).

6.1. The Slopes of the Intrinsic Rates per Mass Bin at Low Redshift

In Figure 8, we show how the intrinsic BBH merger rate density, $R_{\rm BBH}(z)$, evolves as a function of redshift for four different $M_{\rm BH,1}$ mass bins. In each mass bin, we have normalized the merger rate to the rate at redshift zero, to emphasize different trends at low redshifts. We see clear differences in the evolution of the rate at low redshift and the overall redshift evolution. These differences are highlighted by the orange lines, which show linear fits in the range $0 \leqslant z \leqslant 1$, with the slopes a_i provided in the legend.

For the lowest-mass BHs ($M_{\rm BH,1} \leqslant 10\,M_\odot$ and $10\,M_\odot \leqslant M_{\rm BH,1} \leqslant 20\,M_\odot$), our models predict a steep increase of the BBH merger rate density with increasing redshift, with a slope that is very similar to the slope of SFRD(z)/SFRD($z = 0$). The peak of the merger rate of the lowest $M_{\rm BH,1}$ bin coincides with the peak of SFRD(z)/SFRD($z = 0$), as adopted in our models (at $z = 2.7$). The merger rate for slightly higher masses ($10\,M_\odot \leqslant M_{\rm BH,1} \leqslant 20\,M_\odot$) peaks at slightly higher redshifts, around $z = 2.8$. The redshift evolution of $R_{\rm BBH}(z)/R_0$ follows the shape of SFRD(z)/SFRD($z = 0$) for these mass bins, because the lowest-mass events are formed predominantly through the CE channel, which produces short delay-time systems. On top of this, these lower-mass events can form from almost all metallicities, as opposed to the high-mass systems that only form from the lowest metallicities (see Figure 7).

In contrast, for BHs with masses in the range $20\,M_\odot < M_{\rm BH,1} \leqslant 30\,M_\odot$, we find that the evolution of the merger rate with redshift is much less steep in the low-redshift regime than the merger rate for lower-mass BHs. Moreover, the merger rate of these events starts to decline at redshift $z = 2.4$, lower than the redshift of peak SFRD(z). The rate density for the most massive BHs ($M_{\rm BH,1} > 30\,M_\odot$) exhibits the flattest slope and peaks at the lowest redshift (at $z = 1.9$). In other words, in order to capture the peak of the BBH merger rate density for BHs with $M_{\rm BH,1} \gtrsim 30\,M_\odot$, we need gravitational-wave detectors that can observe out to redshift $z \sim 2$ (depending on the exact location of the peak of star formation). This peak at lower redshift can be understood as a result of the characteristics of the stable RLOF channel, which is the primary producer of such massive events. As discussed in Sections 3 and 5, these events primarily form with long delay times. Hence, at progressively higher redshifts, the fraction of systems formed through the stable RLOF channel BBHs that can contribute to the merger rate decreases. The systems that do not contribute at higher redshift have not had sufficient time since the adopted moment of first star formation to merge as a BBH.

This implies that mergers of massive BHs are relatively less common at higher redshifts. This may seem counterintuitive at first sight, considering that at higher redshifts, the low metallicities that allow for the formation of massive BHs are more common (see Figure 7 and, e.g., Vink & de Koter 2005; Belczynski et al. 2010; Spera et al. 2019).

6.2. Observing the Different Slopes in GWTC-2

To test our prediction of a distinct redshift evolution for different $M_{\rm BH,1}$ as discussed in Section 6.1, we look for observational evidence of a different slope in $R_{\rm BBH}(z)$ in the open data from the first, the second, and half of the third

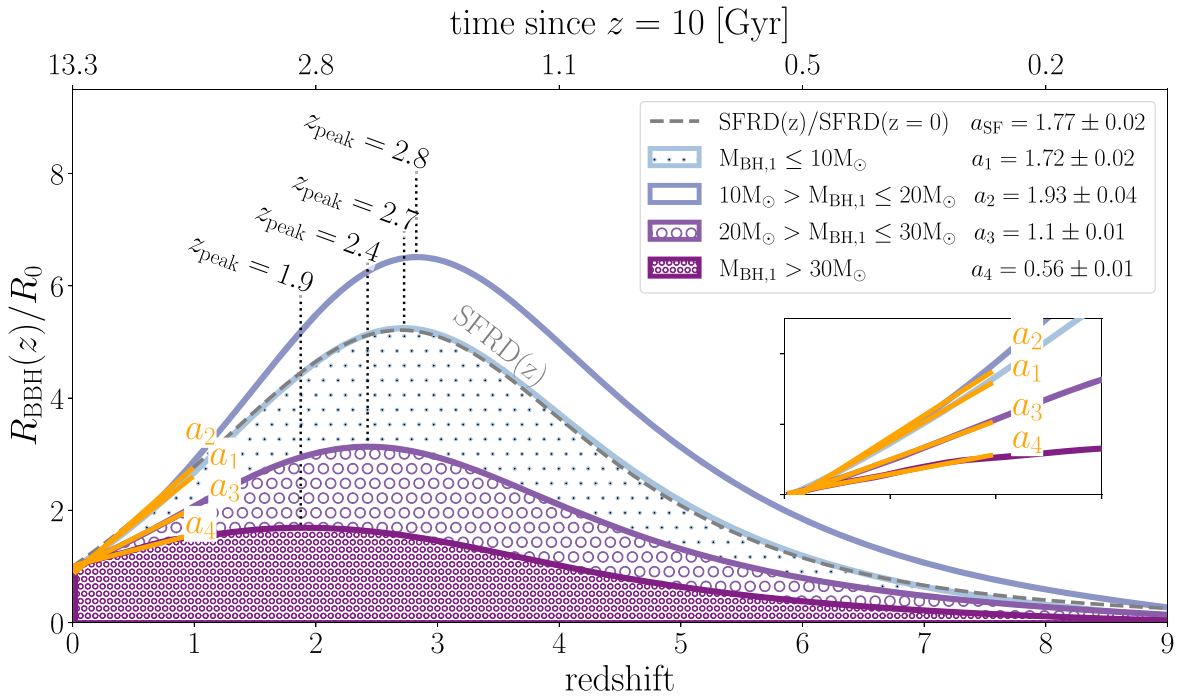

Figure 8. Intrinsic BBH merger rate density as a function of redshift, z ($R_{\rm BBH}(z)$; see Equation (2)), normalized by the rate at redshift zero (R_0), for several bins in primary BH mass. The top axis shows the time since $z = 10$, which we have chosen as the redshift of first star formation. The dashed gray line shows the star formation rate density as a function of redshift, SFRD(z), normalized by the star formation rate density at redshift 0, SFRD($z = 0$). The redshift at which the merger rate peaks is annotated with a dotted line for each mass bin. A linear fit to the merger rate density between $0 \leqslant z \leqslant 1$ is shown with an orange line for each mass bin (these are also highlighted in the inset). The respective slopes of these fits are annotated in the legend. This shows that, at low redshift, the slope of $R_{\rm BBH}(z)$ is more shallow for higher $M_{\rm BH,1}$.

observing runs of Advanced LIGO and Advanced Virgo (Abbott et al. 2021e), also presented in the gravitational-wave transient catalogs GWTC-2 (Abbott et al. 2021g) and GWTC-2.1 (Abbott et al. 2021f). To this end, we use the observed BBH mergers to hierarchically infer their underlying mass and spin distributions (e.g., Mandel et al. 2019).

Contrary to our predictions here, analyses of the BBH population typically assume that BBHs have independently distributed masses and redshifts, with $p(M_{\rm BH,1}, z) = p(M_{\rm BH,1})p(z)$. Here, we will explore several alternative models for the joint distribution $p(M_{\rm BH,1}, z)$ of BBH masses and redshifts. Our method closely follows that of Callister et al. (2021). We assume that the distribution of mass ratios $p(q|M_{\rm BH,1}, \gamma)$ follows a power law with index γ and that the distribution of effective spins, $p(\chi_{\rm eff}|\mu_\chi, \sigma_\chi)$, follows a Gaussian with mean μ_χ and variance σ_χ (Roulet & Zaldarriaga 2019; Miller et al. 2020).

For primary masses and redshifts, we take as a baseline the POWERLAW + PEAK model from Abbott et al. (2021d), with an overall merger rate that is allowed to evolve as a function of z:

$$\frac{dN_{\rm BBH}}{dt\, dM_{\rm BH,1} dz} = R_0 \frac{dV_c}{dz}(1+z)^\kappa [f_p P(M_{\rm BH,1}|\lambda, m_{\rm max}) + (1-f_p) N(M_{\rm BH,1}|\mu_m, \sigma_m, m_{\rm max})]. \quad (7)$$

Here, the assumed primary mass distribution is a mixture between a power law $P(M_{\rm BH,1}|\lambda, m_{\rm max}) \propto M_{\rm BH,1}^\lambda$ (for $M_{\rm BH,1}$ between $5\,M_\odot$ and $m_{\rm max}$) and a Gaussian peak $N(M_{\rm BH,1}|\mu_m, \sigma_m, m_{\rm max})$, with mean μ_m and variance σ_m, which is needed to fit an observed excess of BBHs with primary masses near $M_{\rm BH,1} \approx 35\,M_\odot$. R_0 is the local rate of BBH mergers per comoving volume at $z = 0$.

We inspect several variations of this model in an attempt to identify any relationship between BBH masses and their redshift distribution.

First, we expanded Equation (7) such that the parameter κ, governing the BBH rate evolution, is a function of $M_{\rm BH,1}$. We considered several possibilities, including a piecewise function cut at $30\,M_\odot$,

$$\kappa(M_{\rm BH,1}) = \begin{cases} \kappa_{\rm low} & (M_{\rm BH,1} < 30\,M_\odot) \\ \kappa_{\rm high} & (M_{\rm BH,1} \geqslant 30\,M_\odot), \end{cases} \quad (8)$$

a piecewise function in which the cut location $m_{\rm cut}$ itself varies as a free parameter,

$$\kappa(M_{\rm BH,1}|m_{\rm cut}) = \begin{cases} \kappa_{\rm low} & (M_{\rm BH,1} < m_{\rm cut}) \\ \kappa_{\rm high} & (M_{\rm BH,1} \geqslant m_{\rm cut}), \end{cases} \quad (9)$$

and a case in which κ is a linear function of $M_{\rm BH,1}$:

$$\kappa(M_{\rm BH,1}|\kappa_0, \kappa') = \kappa_0 + \kappa' \left(\frac{M_{\rm BH,1}}{30\,M_\odot} - 1 \right). \quad (10)$$

In Figure 8, we also saw that $dR_{\rm BBH}/dz$ is not a strictly monotonic function of mass. Instead, this slope reaches a maximum in the range $10\,M_\odot < M_{\rm BH,1} \leqslant 20\,M_\odot$, below which it again decreases. To capture this possibility, we additionally considered a *three*-bin piecewise model:

$$\kappa(M_{\rm BH,1}) = \begin{cases} \kappa_{\rm low} & (M_{\rm BH,1} < 10\,M_\odot) \\ \kappa_{\rm mid} & (10\,M_\odot \geqslant M_{\rm BH,1} < 30\,M_\odot). \\ \kappa_{\rm high} & (M_{\rm BH,1} \geqslant 30\,M_\odot) \end{cases} \quad (11)$$

We do not consider more complex models, given the relative scarcity of the data available at the time of writing. In all four cases above, we find no evidence for a varying redshift distribution as a function of mass.

As mentioned above, the BBH primary mass distribution in GWTC-2 is well-modeled as a mixture between a broad power law and an additional peak between 30 and 35 $M_\odot$. As an alternative test, we allow the rates of BBHs comprising the broad power law and those situated in the peak to each evolve independently as a function of redshift:

$$\frac{dN_{\rm BBH}}{dt\, dM_{\rm BH,1} dz} = \frac{dV_c}{dz}[R_0^{\rm pl}(1+z)^{\kappa_{\rm pl}} P(M_{\rm BH,1}|\lambda, m_{\rm max}) + R_0^{\rm peak}(1+z)^{\kappa_{\rm peak}} N(M_{\rm BH,1}|\mu_m, \sigma_m, m_{\rm max}).], \quad (12)$$

in which $R_0^{\rm pl}$ and $R_0^{\rm peak}$ are the local merger rate densities of BBHs in the power law and peak, respectively, with $\kappa_{\rm pl}$ and $\kappa_{\rm peak}$ governing the redshift evolution of each rate. We find very marginal evidence that the BBH mergers comprising these two components obey different redshift distributions; we measure $\kappa_{\rm pl} = 2.7^{+3.2}_{-3.5}$ and $\kappa_{\rm peak} = 0.7^{+4.0}_{-5.8}$, with $\kappa_{\rm peak} < \kappa_{\rm pl}$ for about 70% of the posterior samples. However, our large uncertainties mean we cannot draw any conclusions about differing rate evolution (or lack thereof).

We conclude that we find insufficient evidence in GWTC-2 (Abbott et al. 2021g) for a distinct redshift evolution of $R_{\rm BBH}(z)$ for different $M_{\rm BH,1}$. This is consistent with Fishbach et al. (2021), who find no strong evidence in GWTC-2 that the BBH mass distribution evolves with redshift. Specifically, they find that the detections in GWTC-2 are consistent with a mass distribution that consists of a power law with a break that does *not* evolve with redshift, as well as with a mass distribution that includes a sharp maximum mass cutoff, if this cutoff *does* evolve with redshift. Furthermore, Fishbach & Kalogera (2021) found no strong evidence for the time-delay distribution to evolve with mass. They did find a mild preference for high-mass ($M_{\rm BH,1} \sim 50\,M_\odot$) BBH systems to prefer shorter delay times than the low-mass ($M_{\rm BH,1} \sim 15\,M_\odot$) BBH systems. However, they also argue that this preference could be an effect of higher-mass BHs forming more strictly at the lowest metallicities (which is consistent with our findings in Figure 7). Alternatively, these high-mass mergers with masses of about 50 $M_\odot$ could be probing hierarchical mergers.

At the time of writing, finding evidence for a distinct redshift evolution in GWTC-2 is difficult, considering that observed BBHs with lower-mass primary BH masses ($M_{\rm BH,1} \sim 10\,M_\odot$) only probe the very local universe ($z \lesssim 0.4$). As can be seen from Figure 8, this redshift range encompasses only a small fraction of the BBH merger rate evolution. Given the prospects of observing BBH mergers out to increasingly high redshifts with Advanced LIGO, Advanced Virgo, and KAGRA (Abbott et al. 2018), as well as second- (Voyager Adhikari et al. 2020) and third-generation detectors like the Einstein telescope (Punturo et al. 2010; Hild et al. 2011; Sathyaprakash et al. 2019b; Maggiore et al. 2020) and the Cosmic Explorer (Abbott et al. 2017; Reitze et al. 2019), we expect our predicted different evolution of the BBH merger rate to be either confirmed or disproved within the coming decades.

7. Discussion

In the previous sections, we predicted that the mass distribution of merging BBH systems varies with redshift. Specifically, we showed that the evolution of the merger rate with redshift, $R_{\rm BBH}(z)$, is more shallow and peaks at lower redshifts for systems with higher primary BH masses compared to systems with lower primary BH masses. This difference is the result of the contribution of two different formation channels. The CE channel predominantly forms lower-mass BBH systems ($M_{\rm BH,1} \lesssim 30\,M_\odot$) and allows for very short delay times ($t_{\rm delay} < 1$ Gyr). In contrast, the stable RLOF channel is the main source of massive systems ($M_{\rm BH,1} \gtrsim 30\,M_\odot$) and primarily forms systems with longer delay times ($t_{\rm delay} \gtrsim 1$ Gyr).

The quantitative predictions presented in this work are subject to several major uncertainties, and we discuss the key ones in the remainder of this section. Throughout this section, we also argue why we expect our qualitative findings to be robust.

7.1. The Relative Contribution of the CE and Stable RLOF Channel

The prediction that merging BBHs can be formed through both the CE and stable RLOF channels has been reported by various groups (e.g., van den Heuvel et al. 2017; Bavera et al. 2021; Marchant et al. 2021; Broekgaarden et al. 2021a; Gallegos-Garcia et al. 2021; Shao & Li 2021; Olejak et al. 2021). However, the relative contributions of both channels are uncertain. This is mainly due to uncertainties in the treatment of stability of mass transfer, and whether or not the ejection of a common envelope is successful (Ivanova et al. 2013, 2020, and references therein).

Recent works by, e.g., Pavlovskii et al. (2017), Klencki et al. (2021), Marchant et al. (2021), and Gallegos-Garcia et al. (2021) have questioned whether the CE channel plays a prominent role, based on results obtained with the 1D detailed binary evolutionary code MESA (Paxton et al. 2015). They argue that systems that are typically assumed to lead to successful CE ejection in rapid population synthesis simulations (such as ours) will instead fail to initiate and survive a common envelope phase. If true, this potentially could drastically reduce the relative contribution of the CE channel. This would have major implications for the field and implies that the contribution of the CE channel is overestimated in our work.

Despite all of the above, it seems unlikely that the CE channel does not operate at all. Various compact binary systems containing double white dwarfs and double neutron stars exist, which are hard to explain through other formation channels (Rebassa-Mansergas et al. 2007, 2012; Nebot Gómez-Morán et al. 2011; Ivanova et al. 2013). As long as the CE channel plays a non-negligible role, we believe that at least our qualitative conclusions will hold.

7.2. Are the Delay Time and Mass Distributions of the Two Channels Distinguishable?

Although the detailed shape of the delay time and mass distributions are uncertain, we believe that our finding that these two channels lead to distinct delay-time distributions is robust for the following reasons.

The first reason is that the CE channel and stable RLOF channel lose angular momentum through intrinsically different mechanisms, as explained in Section 3.2. Because of this, it is reasonable to expect a difference in the distributions of final separations and thus inspiral times. In fact, fine tuning would be required to avoid significant differences. Similar arguments can be made for the mass distribution (see, e.g., Dominik et al. 2012; Eldridge & Stanway 2016; Bavera et al. 2021; Gallegos-Garcia et al. 2021).

To better understand the impact of our (uncertain) model assumptions on the resulting delay time and mass distributions, we have analyzed the suite of models presented in Broekgaarden et al. (2021b) (see Appendix F). A relative lack of high-mass BHs with short delay times was found in all model variations. Furthermore, we find significant differences in the delay-time and mass distributions for the two channels for almost all variations.

Exceptions concern the models where we assume high values for the CE ejection efficiency $\alpha_{\rm CE}$ (panels H and I in Figure 14). In these simulations, the number of short delay-time systems resulting from the CE channel is reduced (for $\alpha_{\rm CE}=2$) or they disappear entirely (for $\alpha_{\rm CE}=10$). The latter assumption results in delay-time distributions for the CE and RLOF channel that are practically indistinguishable, but we consider such high efficiencies unrealistic.

The distinction in the $M_{\rm BH,1}$ distribution diminishes in the models where a fixed accretion efficiency during stable Roche-lobe overflow involving two stellar companions is considered, $\beta=0.25$ and $\beta=0.5$, where β denotes the fraction of the mass lost by the donor that is accreted by the companion (see panels B and C in Figure 14). In these models, we find that the RLOF channel is less efficient at producing BBH mergers, especially in the case of systems with high-mass $M_{\rm BH,1}$. We still find significant differences in the delay times between the two channels, but the RLOF and CE channel can no longer be clearly distinguished in the $M_{\rm BH,1}$ distribution. While the efficiency of mass accretion is an important uncertainty in our simulations, we do not believe that assuming a fixed accretion efficiency is realistic.

7.3. Alternative Observables to Distinguish the Two Channels

We are not able to directly observe whether a BBH was formed through the CE channel or the stable RLOF channel. Hence, we need characteristic observable source properties to expose the distinct rate evolution. In this work, we have focused on BH mass, as this can be inferred relatively well from observations. Possible other observables that could be used are the distribution of the BH spins, the secondary masses, and the mass ratio.

Mass ratios—In the left panel of Figure 9, we show our predictions for the distribution of mass ratios as seen by a hypothetical perfect detector (Equation (6)); these predictions are very different for each channel. The CE channel preferentially produces systems with unequal masses ($q_{\rm final}\approx 0.3$), but the distribution is broad and spans from $0.2\lesssim q_{\rm final}\lesssim 1$. In contrast, we find that the stable RLOF channel predominantly forms merging binaries with $0.6\lesssim q_{\rm final}\lesssim 0.8$ in our simulation. The distinct shape of this distribution is the result of the requirement of the stability of mass transfer, the relation of total mass to core mass, and the efficiency of mass transfer (see Appendix A for an analytical derivation of the low $q_{\rm final}$ end). The clear difference in the two distributions is promising, but we note that, at the time of this writing, the mass ratios inferred for the detected systems are typically not well-constrained (e.g., Abbott et al. 2021a).

Secondary masses—The distribution of secondary masses, $M_{\rm BH,2}$, is shown in the right panel of Figure 9. The CE channel dominates the formation of low secondary BH masses $M_{\rm BH,2}<15\,M_\odot$, while the stable RLOF channel dominates in the range $15\,M_\odot<M_{\rm BH,2}<40\,M_\odot$. The reason for this is the same as discussed in Section 3.1. The CE channel dominates again for the BHs with the highest secondary masses ($36\,M_\odot<M_{\rm BH,2}<46\,M_\odot$). The contribution of the stable RLOF drops quickly here, due to a lack of equal-mass systems and the PISN mass limit of about $46\,M_\odot$. We caution that the features of the highest-mass BHs should not be overinterpreted, as the uncertainties in the evolution of the progenitor systems are the largest here.

Spins–Gravitational-wave observations provide constraints on the mass-weighted effective spin, $\chi_{\rm eff}$, and for some events on the individual spin magnitudes and their orientations. The constraints on the spin have been suggested as a promising diagnostic to distinguish formation scenarios (e.g., Kushnir et al. 2016; Hotokezaka & Piran 2017; Zaldarriaga et al. 2018).

Our simulations do not provide predictions for the spin, but Bavera et al. (2020) showed that, in the case of the CE channel, the post-CE separation may well be small enough to allow for tidal spin-up of the He core that is the progenitor of the second born BH (e.g., Bavera et al. 2020; Mandel & Fragos 2020). In the case of the stable RLOF channel, final separations are expected to be too wide for tidal spin-up (e.g., Bavera et al. 2021), but one might expect spin-up of the firstborn BH through mass transfer (e.g., Bardeen 1970), although this is a matter of debate. In case of Eddington-limited accretion, spin-up may not be significant (Bavera et al. 2021). In the case of super-Eddington accretion, it remains unclear whether one can significantly spin up the accreting BH (e.g., Tchekhovskoy et al. 2012), and in this case the orbit widens, preventing the formation of a GW source (van Son et al. 2020). Furthermore, large uncertainties remain in the angular momentum transport of massive stars, which makes it difficult to accurately translate stellar spins to BH spins (see, e.g., Fuller et al. 2015; Olejak & Belczynski 2021; and Steinle & Kesden 2021, for a discussion of possible pathways to spinning BHs from the isolated binary channel).

7.4. The Uncertain Metallicity-dependent Cosmic Star Formation History

In general, variations in the assumed $\mathcal{S}(Z,z)$ have a large impact on $R_{\rm BBH}(z)$ and the shape of the BH mass distribution (e.g., Chruślińska et al. 2018; Neijssel et al. 2019; Broekgaarden et al. 2021b; Briel et al. 2021). Because the highest-mass BHs can only form from the lowest metallicities (see Figure 7), the stable RLOF channel will only play a significant role in the BBH merger rate if there is sufficient star formation at low metallicity and the stable RLOF systems have had enough time to coalesce since this low-metallicity star formation.

To test the effect of the $\mathcal{S}(Z,z)$ on our main results, we repeated our complete analysis while adopting the phenomenological model from Neijssel et al. (2019). This $\mathcal{S}(Z,z)$ forms fewer stars at low metallicity ($Z<0.01$) for the majority of our simulated star-forming universe, but forms a significantly larger amount of low-metallicity stars at the highest redshifts. Because this model is very sharply peaked around the mean

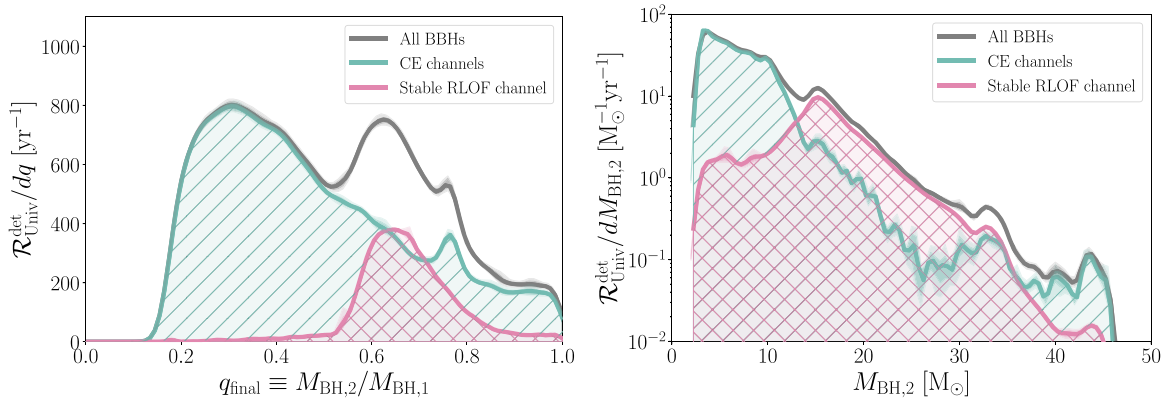

Figure 9. Distributions of mass ratios, $q_{\rm final}$, and secondary masses, $M_{\rm BH,2}$, for BBHs seen by a hypothetical perfect detector ($\mathcal{R}^{\rm det}_{\rm Univ}(\zeta)$; Equation (6)). Each panel shows the distribution for all systems in gray, the stable RLOF channel in cross-hatched pink, and the CE channel in line-hatched green. The dark and light shaded areas show the 1 and 2σ sampling uncertainties, respectively, obtained through bootstrapping.

metallicity at each redshift, there is almost no star formation at low metallicities for all redshifts lower than $z \approx 1$. In contrast, in our fiducial model, we adopt a skewed distribution to capture the tail of low-metallicity star formation at low redshifts. With this $\mathcal{S}(Z, z)$, we still retrieve a distinct redshift evolution for different BH mass bins, similar to the trends discussed in Sections 5 and 6. Specifically, we find a steep positive slope for $R_{\rm BBH}(z)$ between $0 < z < 1$ for BBHs with $M_{\rm BH,1} < 20\,M_\odot$, and a more shallow slope for BBHs with $M_{\rm BH,1} \geqslant 20\,M_\odot$. This causes the high-mass end ($M_{\rm BH,1} \gtrsim 20\,M_\odot$) of the $M_{\rm BH,1}$ mass distribution to decay faster at higher redshifts than the low-mass end ($M_{\rm BH,1} \lesssim 18\,M_\odot$) of the distribution. This is in line with Neijssel et al. (2019), who also found evidence for evolution of the BBH mass distribution with redshift.

Our estimate of the total intrinsic BBH merger rate is $R_0 = 73\,{\rm Gpc^{-3}\,yr^{-1}}$ at redshift zero, and $R_{0.2} = 94\,{\rm Gpc^{-3}\,yr^{-1}}$ at $z = 0.2$. Although this rate prediction is not an outlier in the recent review of local BBH merger rate predictions for isolated binaries from Mandel & Broekgaarden (2022), it is a factor of 2–5 higher than the most recent estimates from the LIGO/Virgo/Kagra collaboration ($R_{0.2} = 17.3$–$45\,{\rm Gpc^{-3}\,yr^{-1}}$; see Abbott et al. 2021b). Our setup and binary physics assumptions are similar to those in Neijssel et al. (2019), who predict a local rate of $R_0 \approx 22\,{\rm Gpc^{-3}\,yr^{-1}}$. The difference in our rate prediction stems from our updated prescription for the metallicity-dependent star formation rate density as described above, $\mathcal{S}(Z, z)$ (see also Appendix C).

Although we acknowledge the large uncertainties in $\mathcal{S}(Z, z)$, we note that, if we are sufficiently confident in the delay time distributions of observed BBH mergers, the redshift evolution of the BBH merger rate can be used to measure the star formation rate with gravitational waves (Vitale et al. 2019). Therefore, detecting evolution in the BH mass distribution as described in Section 6 could help us constrain $\mathcal{S}(Z, z)$ through gravitational waves.

7.5. Further Caveats of Rapid Population Synthesis

All uncertainties that apply to rapid population synthesis simulations also apply to this work (see, e.g., Ablimit & Maeda 2018; Belczynski et al. 2022; Broekgaarden et al. 2021b). Above, we already discussed the main uncertainties related to mass-transfer stability and the treatment of common envelope phases. Below, we highlight further known shortcomings and uncertainties that are expected to impact our quantitative predictions.

A major uncertainty for the evolution of massive stars concerns internal mixing, and specifically, mixing beyond the boundaries of the convectively unstable regions. This directly impacts the core masses. In our simulations, we use prescriptions from Hurley et al. (2000) that are fitted against models by Pols et al. (1997). For stars with initial masses higher than $50\,M_\odot$, these fits are extrapolated. The core masses in our simulations turn out to be substantially smaller than those predicted in more recent grids of detailed evolutionary models that were calibrated against observations (e.g., Brott et al. 2011). Overall, we expect our core masses for high-mass stars to be underestimated (as is true for all simulations that apply the original Hurley formulae). This will affect the quantitative predictions for the BH mass, as well as the mass ratio distributions. This includes our predictions for the maximum BH mass that is efficiently formed through the CE channel ($\sim 30\ M_\odot$ in this work).

The post-supernova remnant mass, including the amount of fallback, is uncertain. In particular, stars that retain a significant fraction of their envelope up to the moment of core collapse have been hypothesized to produce massive BHs if the envelope is assumed to entirely fall back onto the newly formed BH (e.g., Fernández et al. 2018; Di Carlo et al. 2019, 2020). This way, relatively low-mass stars ($M_{\rm ZAMS} \lesssim 40\,M_\odot$) that are expected to more easily lead to successful CE events (following our arguments as stated in Section 3.1) can still form high BH masses ($M_{\rm BH,1} \gtrsim 30\,M_\odot$; see Di Carlo et al. 2019, 2020 Kremer et al. 2020). However, for red supergiant stars, the envelope is expected to be sufficiently loosely bound that the change in gravitational mass due to neutrino losses when a core collapses likely unbinds the envelope (Nadezhin 1980; Lovegrove & Woosley 2013; Adams et al. 2017). Complete fallback is expected only for blue and yellow supergiants (Fernández et al. 2018; Ivanov & Fernández 2021). Moreover, in this work we only study isolated binaries, which are not able to form BBH progenitors that merge within the age of the universe without the system transferring or losing angular momentum as a consequence of mass transfer. Mass transfer, whether stable or unstable (CE), leads to significant mass loss in our simulations. Therefore, we find that forming merging BBHs with a massive primary BH through the fallback of a hydrogen envelope only works if there is an

external mechanism that brings the BH progenitors closer together.

Finally, in this work we have assumed a universal initial mass function (IMF). However, recent studies suggest that the IMF might be more top-heavy at low metallicity (e.g., Geha et al. 2013; Martín-Navarro et al. 2015; Schneider et al. 2018; Gennaro et al. 2018). Although uncertainties in the IMF can have a large impact on rate predictions (de Mink & Belczynski 2015; Chruślińska et al. 2021), to first order, we expect to still retrieve distinct redshift evolutions, $R_{\rm BBH}(z)$, for low- and high-mass BHs, because the existence of the CE channel and that of the stable RLOF channel are not affected by IMF changes. A full study of the effect of a nonuniversal IMF is outside the scope of this paper.

7.6. Contribution from Other Formation Channels

In this work, we focus on predictions from the isolated binary channel. However, the observed population of merging BBHs is most likely a mixture of several channels (Zevin et al. 2021; Wong et al. 2021). The variety of physics involved is vast, and hence the span of predictions for merging BBH properties is equally large. See also Mapelli et al. (2021) and Mandel & Farmer (2022) for reviews of proposed formation channels, and Mandel & Broekgaarden (2022) for a review of predictions for the merger rates from said formation channels. Below, we summarize findings for other formation channels, with an emphasis on delay-time predictions, the slope of $R_{\rm BBH}(z)$, and the predicted mass distribution (see also Fishbach & Kalogera 2021 for an overview of delay-time predictions from several different formation channels).

Two formation channels that exhibit a preference for the formation of more massive BBHs are chemically homogeneous evolution (CHE; e.g., de Mink et al. 2009; Song et al. 2013, 2016; Mandel & de Mink 2016; Marchant et al. 2016; Riley et al. 2021) and Population III binaries (e.g., Marigo et al. 2001; Belczynski et al. 2004; Kinugawa et al. 2014; Inayoshi et al. 2017). Riley et al. (2021) find that CHE binaries have quite short delay times (between 0.1 and 1 Gyr), causing the redshift evolution of $R_{\rm BBH}(z)$ to be fairly similar between CHE binaries and the full population of isolated binaries. Furthermore, du Buisson et al. (2020) find that the intrinsic BBH merger rate from CHE binaries evolves less steeply at low redshift than their adopted SFRD. Ng et al. (2021) compare the intrinsic BBH merger rate density from formation in isolated binaries and dynamical formation in globular clusters to predictions for BBH mergers formed from Population III stars. They find that Population III remnants should result in a secondary peak of $R_{\rm BBH}(z)$ around $z \approx 12$ (beyond what we have adopted as the redshift of first star formation).

Several formation channels have been proposed where the BBH merger is assisted by dynamical encounters. These include BBH formation in nuclear star clusters (e.g., Antonini et al. 2016; Petrovich & Antonini 2017; Antonini et al. 2019; Arca Sedda 2020a; Arca Sedda et al. 2020b; Fragione & Silk 2020), globular clusters (e.g., Downing et al. 2010; Bae et al. 2014; Askar et al. 2017; Fragione & Kocsis 2018; Rodriguez et al. 2019), and young stellar clusters (e.g., Portegies Zwart & McMillan 2000; Mapelli et al. 2013; Ziosi et al. 2014; Mapelli et al. 2017; Bouffanais et al. 2019; Fragione & Banerjee 2021). For globular clusters, Choksi et al. (2019) find a merger rate that is weakly increasing out to $z = 1.5$ and drops at higher redshift. This behavior is driven by dynamical processes within the cluster, which introduce a significant delay between cluster formation and BBH mergers.

Recent studies aim to compare the redshift evolution of the intrinsic BBH merger rate between different formation channels. Zevin et al. (2021) investigate the local source properties for the CE channel, stable RLOF channel, globular clusters, and nuclear clusters. Their Figure 1 shows evidence that the stable RLOF channel preferentially forms higher chirp masses than the CE channel. Mapelli (2021) compares the rate evolution of the intrinsic BBH merger rate from isolated binaries to the rate from nuclear star clusters, globular star clusters, and young stellar clusters. Mapelli finds that the primary BH mass function is more top-heavy at high redshift for both globular and nuclear star clusters. In contrast to our work, Mapelli finds that the mass distribution from isolated binaries does not vary greatly with redshift, because the majority of systems in the isolated binary channel studied in that work is formed through CE, which results in short delay times. However, the mass distribution of isolated binaries in Figure 5 of Mapelli (2021) appears to contain fewer primary BH masses of $\gtrsim$20 $M_\odot$ at redshift 4 relative to redshift 0 (although this effect is smaller than the variation with redshift that is retrieved for nuclear and globular clusters in that work).

Finally, AGN disks (e.g., Baruteau et al. 2011; Bellovary et al. 2016; Leigh et al. 2018; Yang et al. 2019; Secunda et al. 2019; McKernan et al. 2020) and mergers in hierarchical systems assisted by dynamical interactions (e.g., Kimpson et al. 2016; Antonini et al. 2017; Rodriguez & Antonini 2018; Hoang et al. 2018) have also been proposed as promising formation channels for BBH mergers.

At the time of this writing, the estimates for the relative contribution of formation channels are highly uncertain. However, linking source properties to predictions for the rate evolution with redshift, such as in this work, could help distinguish between the many possible origins of merging BBH systems.

8. Conclusions and Summary

We discuss the implications of relations between the delay time and BH mass for BBH systems that originate from isolated binaries. We explore the origin of these relations by dividing our simulations into two main formation channels: BBH systems that have experienced at least one common envelope (the "CE channel") and systems that did not experience a CE, i.e., that only experienced stable Roche-lobe overflow (the "stable RLOF channel"). We discuss how our findings affect the redshift evolution of the BBH mass distribution. Specifically, we find a distinct redshift evolution of the BBH merger rate, $R_{\rm BBH}(z)$, for different primary BH masses, $M_{\rm BH,1}$. Below, we summarize our main findings.

The CE channel predominantly forms BBH systems with masses $M_{\rm BH,1} \lesssim 30\,M_\odot$ and typically short delay times ($t_{\rm delay} < 1$ Gyr)—The CE channel typically leads to shorter separations at BBH formation than the stable RLOF channel. On average, this causes shorter inspiral times and thus shorter delay times (Figure 2). The CE channel does not form more massive BHs, because the massive progenitor stars required for these BH masses experience less radial expansion and stronger winds with respect to their lower-mass counterparts. This results in conditions that are ill-favored for successful common-envelope initiation and ejection.

The stable RLOF channel generally forms BBH systems with longer delay times ($t_{\rm delay} \gtrsim 1$ Gyr), and it is the main source of BBH systems with $M_{\rm BH,1} \gtrsim 30\,M_\odot$.—The stable RLOF channel primarily produces larger separations at BBH formation than the CE channel, resulting in longer delay times. Because high-mass stars are ill-favored for successful common-envelope initiation and ejection, the highest-mass BHs are almost exclusively formed through the stable RLOF channel.

The redshift evolution of the intrinsic BBH merger rate density is different for low and high $M_{\rm BH,1}$—Due to the relations between the delay time and BH mass, we find distinctly different slopes in the BBH merger rate density $R_{\rm BBH}(z)$ for different mass ranges of $M_{\rm BH,1}$ (see Figure 8). The merger rate density of the lowest-mass BHs ($M_{\rm BH,1} \leqslant 20\,M_\odot$) is dominated by the CE channel. For these BH masses, the merger rate density has a slope at low redshift that is similar to the slope of the star formation rate. The merger rate density of the highest-mass BHs ($M_{\rm BH,1} \geqslant 30\,M_\odot$) is dominated by the stable RLOF channel. These higher-mass systems have relatively longer delay times ($t_{\rm delay} > 1$ Gyr), causing the rate density to peak at lower redshift than the peak of the star formation rate. We find that, in the low-redshift regime that current detectors probe, the evolution of the merger rate density is less steep for higher-mass $M_{\rm BH,1}$ than for lower-mass BHs.

Although we cannot find significant evidence for this relation in the observed data at the time of writing, if isolated binaries contribute significantly to the BBH merger rate density, we expect that the distinct redshift evolution of the intrinsic merger rate density for different BH masses will be verifiable with near-future detectors (see Section 6.2).

The contribution of different formation channels to $R_{\rm BBH}(z)$ varies with redshift.—While the CE channel dominates the production of merging BBHs in the universe, we predict that almost half of the systems we see merging at redshift 0 come from the stable RLOF channel (Figure 4). Conversely, in the high-redshift universe, the contribution to $R_{\rm BBH}(z)$ from the stable RLOF channel will be negligible.

We thank Charlie Conroy and Eva Laplace for useful discussions and support. We thank Will Farr for his suggestion to investigate trends in the rate per mass bin, and Maya Fishbach for discussing the impact of the results at an early stage. The authors thank Lokesh Khandelwal for his invaluable work on STROOPWAFEL. The authors are furthermore grateful for stimulating conversations with and Katie Breivik and members of the BinCosmos, COMPAS, CCA-GW, and MPA stellar groups. L.v.S. performed portions of this study as part of the remote pre-doctoral Program at the Center for Computational Astrophysics of the Flatiron Institute, supported by the Simons Foundation. L.v.S. and S.d.M. also acknowledge KITP for hospitality. The authors acknowledge partial financial support from the National Science Foundation under grant No. (NSF grant No. 2009131 and PHY-1748958),” the Netherlands Organisation for Scientific Research (NWO) as part of the Vidi research program BinWaves with project number 639.042.728, and the European Union’s Horizon 2020 research and innovation program from the European Research Council (ERC, grant agreement No. 715063). I.M. is partially supported by the Australian Research Council (ARC) Centre of Excellence for Gravitational-wave Discovery (OzGrav), project number CE170100004. I.M. is the recipient of the ARC Future Fellowship FT190100574. This research has made use of NASA’s Astrophysics Data System Bibliographic Services.

Software and Data: The data used in this work are available on Zenodo under an open-source Creative Commons Attribution license at https://doi.org/10.5281/zenodo.5544170. Simulations in this paper made use of the `COMPAS` rapid binary population synthesis code (v02.19.04), which is freely available at http://github.com/TeamCOMPAS/COMPAS (Riley et al. 2022). The data used in Appendix F are described in Broekgaarden et al. (2021b) and are publicly available at https://zenodo.org/record/5651073. The authors use the adaptive importance sampling tool STROOPWAFEL from Broekgaarden et al. (2019), publicly available at https://github.com/lokiysh/stroopwafel.

This research has made use of GW data provided by the Gravitational Wave Open Science Center (https://www.gw-openscience.org/), a service of LIGO Laboratory, the LIGO Scientific Collaboration, and the Virgo Collaboration. LIGO Laboratory and Advanced LIGO are funded by the United States National Science Foundation (NSF) as well as the Science and Technology Facilities Council (STFC) of the United Kingdom, the Max-Planck-Society (MPS), and the State of Niedersachsen/Germany for support of the construction of Advanced LIGO and construction and operation of the GEO600 detector. Additional support for Advanced LIGO was provided by the Australian Research Council. Virgo is funded, through the European Gravitational Observatory (EGO), by the French Centre National de Recherche Scientifique (CNRS), the Italian Istituto Nazionale di Fisica Nucleare (INFN), and the Dutch Nikhef, with contributions by institutions from Belgium, Germany, Greece, Hungary, Ireland, Japan, Monaco, Poland, Portugal, and Spain.

Further software used in this work: Python (van Rossum 1995), Astropy (Astropy Collaboration et al. 2013, 2018), Matplotlib (Hunter 2007), NumPy (Harris et al. 2020), SciPy (Virtanen et al. 2020), `ipython/jupyter` (Perez & Granger 2007; Kluyver et al. 2016), Seaborn (Waskom 2021), and hdf5 (Collette 2013).

Appendix A
Inspecting Mass Ratios

Below, we derive the typical minimum mass ratio of a BBH that forms through the stable RLOF channel, as a function of the uncertain assumptions that go into our population synthesis. We will refer to the star that is more (less) massive at zero-age main sequence (ZAMS) as the primary (secondary) and denote it with the subscript A (B). See Figure 1 for a cartoon example of a stable RLOF system, including a short definition of the symbols as used in this section.

A.1. First Mass Transfer: from the Primary to the Secondary

Since the primary star is more massive, it will evolve on a shorter timescale than the secondary, and thus it will be the first to overflow its Roche lobe. The donor (primary star) typically starts RLOF either at the end of its main sequence, or during H-shell burning, also known as Case A or early Case B mass transfer. We will focus on Case B mass transfer (post-core-H-burning) because, due to the large radial expansion, this is the most common case of mass transfer (e.g., Sana et al. 2012). During this phase of stable mass transfer, the primary star will donate at most its envelope to the secondary star. We neglect

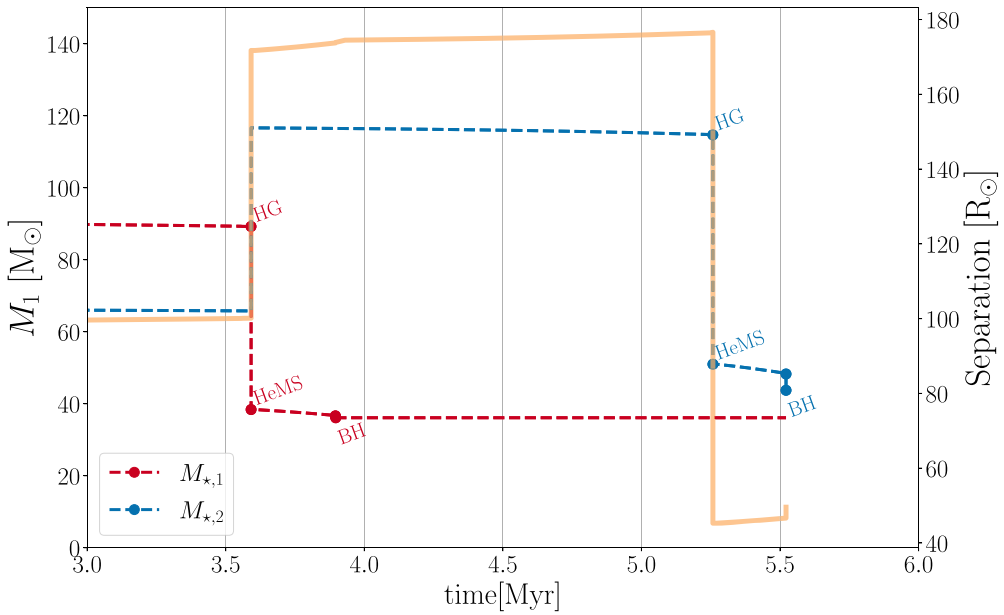

Figure 10. Masses (dashed lines, left *y*-axis) and binary orbital separation (solid yellow line, right *y*-axis) over time, for a typical BBH progenitor system that evolved through the stable RLOF channel. Transitions to different evolutionary stages are labeled with the following acronyms: HG for Hertzsprung-gap star, HeMS for He main-sequence star, and BH for black hole.

all mass loss due to winds in this simple approximation. We capture the mass transfer efficiency in the parameter β, where $\beta = 0$ implies no mass is accreted, while $\beta = 1$ implies the complete envelope of the primary is accreted by the secondary. The mass of the secondary after completion of the first mass-transfer phase becomes:

$$\begin{aligned}\tilde{M}_{\rm B} &= M_{\rm ZAMS,B} + \beta M_{env,A} = M_{\rm ZAMS,A} \cdot q_{\rm ZAMS} \\ &\quad + M_{\rm ZAMS,A} \cdot \beta(1 - f_{\rm core}) \\ &= M_{\rm ZAMS,A} \cdot (q_{\rm ZAMS} + \beta(1 - f_{\rm core})),\end{aligned} \tag{A1}$$

where $q_{\rm ZAMS} \equiv M_{\rm ZAMS,B}/M_{\rm ZAMS,A}$, and we assume a fraction $f_{\rm core}$ of the stellar mass is used to form the He core. We implicitly assume that the respective core mass fractions of star A and star B are similar, i.e., $f_{\rm core,A}/f_{\rm core,B} \approx 1$.

The primary star will continue to evolve and ultimately form a BH. For the purpose of this argument, we assume the complete core mass of the primary goes into forming the BH mass, i.e.,

$$M_{\rm BH,A} = M_{\rm ZAMS,A} \cdot f_{\rm core}\,. \tag{A2}$$

A.2. Second Mass Transfer: from the Secondary to the Primary

When the secondary star ends core-H burning, it will swell up in size, and in our case, start stable mass transfer. The second phase of mass transfer is highly nonconservative, since accretion onto the BH is assumed to be Eddington-limited. Therefore, $M_{\rm BH,A}$ remains approximately the same, and $M_{\rm BH,B}$ will be approximately

$$M_{\rm BH,B} = \tilde{M}_{\rm B} f_{\rm core}\,, \tag{A3}$$

where we again assume that the complete He core mass is used to form the BH mass.

A.3. Final Mass Ratio

We find that, for the stable channel, $M_{\rm BH,B}$ typically forms the more massive BH, because in most cases star B accretes a significant fraction of its companions envelope, making it more massive than the primary at ZAMS. Hence, we define the typical final mass ratio at BBH formation as:

$$q_{\rm final} \equiv \frac{M_{\rm BH,A}}{M_{\rm BH,B}} \approx q_{\rm BBH}. \tag{A4}$$

Using Equations (A2) and (A3), we find

$$q_{\rm BBH} = \frac{M_{\rm ZAMS,A}}{\tilde{M}_{\rm B}} = \frac{1}{(q_{\rm ZAMS} + \beta(1 - f_{\rm core}))}. \tag{A5}$$

We find that, in our simulations, core mass fractions range between about 0.33 and 0.43. To minimize Equation (A5), we further need to maximize $q_{\rm ZAMS} = 1$ and $\beta = 1$. Hence, we find $\min(q_{\rm final}) \approx 0.60$–$0.64$. This agrees broadly with the location of the drop in the distribution of mass ratios that we find in our simulations below around $q_{\rm final} \approx 0.6$, shown in Figure 9. Understanding the right-hand side of the mass ratio distribution is more involved. It is set in part by the requirement that the systems shrinks sufficiently during the second mass transfer, but also by mass transfer efficiency itself.

For illustration, we also show a typical example system in Figure 10. This system starts with $M_{\rm ZAMS,1} \approx 90\,M_\odot$ and $M_{\rm ZAMS,2} \approx 70\,M_\odot$ and ends with $M_{\rm BH,A} = 36\,M_\odot$ and $M_{\rm BH,B} = 43\,M_\odot$, hence $q_{\rm final} \approx 0.84$.

Appendix B
Delay-time Distributions

We emphasize the bimodality in the delay-time distribution by plotting the number of merging BBHs per $\log t_{\rm delay}$ in the left panel of Figure 11. This is similar to Figure 2, but integrated over all BH masses. For completeness, we also

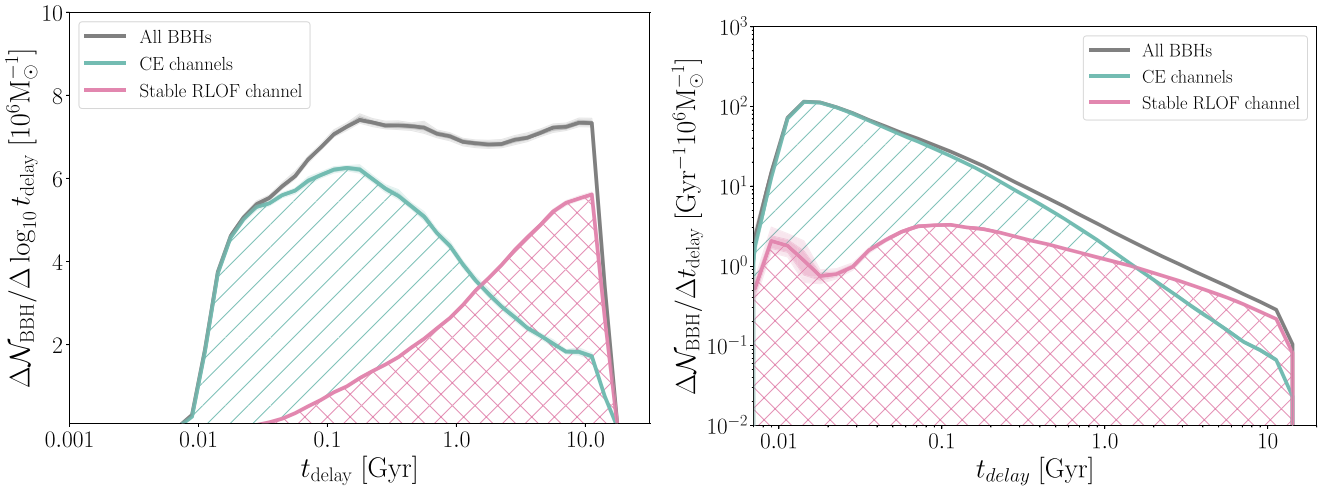

Figure 11. Similar to Figure 2, but integrated over $M_{\rm BH,1}$. The solid line shows the centers of the histogram per $d\log_{10}t_{\rm delay}$ (left panel) vs. the histogram per $dt_{\rm delay}$ (right panel), with bin sizes that are of equal size in log-space ($d\log_{10}t_{\rm delay}=0.1$) and hence unequal size in $t_{\rm delay}$. Both are normalized per $10^6\,M_\odot$ of star-forming mass. This histogram contains a mixture of birth metallicities, which were sampled uniformly in log. The dark and light shaded areas show the 1 and 2σ bootstrapping uncertainties, respectively. We indicate the stable RLOF channel with pink cross-hatched lines, and the CE channel with green line hatches.

show the same distribution, but per $t_{\rm delay}$ (i.e., not in log space).

Appendix C
Metallicity-dependent Star Formation Rate $\mathcal{S}(Z, z)$

Several recent studies have highlighted the importance of the choice of the metallicity-dependent cosmic star formation rate density $\mathcal{S}(Z, z)$ and its impact on the final predictions (e.g., Chruślińska et al. 2019; Chruślińska & Nelemans 2019; Neijssel et al. 2019; Broekgaarden et al. 2021b; Briel et al. 2021).

For the metallicity-dependent star formation history assumed in this work, we use the IllustrisTNG simulations. This is a suite of large magnetohydrodynamical cosmological simulations computed with the moving-mesh code Arepo (Springel 2010; Pakmor et al. 2016; Weinberger et al. 2020). The simulations follow the formation and evolution of galaxies from high redshift to the current time and solve for the evolution of dark matter and gas under the influence of feedback from star formation and supermassive black holes (for details, see Springel et al. 2018; Marinacci et al. 2018; Nelson et al. 2018; Pillepich et al. 2018a; Naiman et al. 2018).

The simulations were originally calibrated against the observed total cosmic star formation rate density and the stellar mass function of galaxies (Pillepich et al. 2018b). They reproduce the evolution of the sizes of galaxies with redshift (Genel et al. 2018) and with observational constraints on the mass–metallicity relation of galaxies up to $z=2$ (Torrey et al. 2019) as well as iron abundances (Naiman et al. 2018) and the metallicity gradients within galaxies at low redshift (Hemler et al. 2021). These simulations have also already been used to make predictions for gravitational-wave sources through pairing with predictions for the outcomes of binary evaluation obtained with the BPASS code Briel et al. (2021).

We extract the amount of star formation ongoing at each redshift and metallicity in the IllustrisTNG100 simulations and use this to derive the metallicity cosmic star formation rate density, $\mathcal{S}(Z, z)$. For this purpose, we make use of an analytical fit inspired by Neijssel et al. (2019) but adapted to better capture the asymmetry in the metallicity distribution as detailed in Van Son et al. (in prep.). For the simulations presented in this work, we use

$$\mathcal{S}(Z,z) = \underbrace{a\frac{(1+z)^b}{1+[(1+z)/c]^d}}_{\text{(1) SFRD}(z)} \times \underbrace{\frac{2}{Z}\phi\left(\frac{\ln Z-\xi(z)}{\omega(z)}\right)\Phi\left(\alpha\frac{\ln Z-\xi(z)}{\omega(z)}\right)}_{\text{(2) } d\mathrm{P}(Z,z)/dZ} \quad [M_\odot\, yr^{-1}\,\mathrm{cMpc}^{-3}], \tag{C1}$$

where the first term (1) governs the overall star formation rate density, SFRD(z), as a function of redshift z (following the analytical form proposed by Madau & Dickinson 2014). The second term (2) governs the metallicity distribution at each redshift; we approximate this with a skewed log-normal distribution written as the product of the standard log-normal distribution, ϕ, and the cumulative distribution function of the standard log-normal distribution, Φ (O'Hagan & Leonard 1976). For the width of the distribution, we assume $\omega(z)=\omega_0\cdot 10^{\omega_z z}$. We furthermore ensure that the mean of the metallicity distribution has the following simple dependence on redshift, $\langle Z\rangle \equiv \mu(z)=\mu_0\cdot 10^{\mu_z z}$, by setting

$$\xi(z)=\frac{-\omega(z)^2}{2}\ln\left(\frac{\mu_0\cdot 10^{\mu_z z}}{2\Phi(\beta\omega(z))}\right) \quad \text{where} \quad \beta=\frac{\alpha}{\sqrt{1+\alpha^2}}. \tag{C2}$$

This leaves us in total with nine free parameters that are fitted simultaneously. In this work, we have used $a=0.02$, $b=1.48$, $c=4.45$, $d=5.9$, $\alpha=-1.77$, $\mu_0=0.025$, $\mu_z=-0.048$, $\omega_0=1.125$, and $\omega_z=0.048$ (see also Van Son et al., in prep).

We note that our approach differs from the approach taken in some earlier studies that use observed scaling relations to construct a prescription for the metallicity-dependent cosmic star formation history, e.g., as proposed by Langer &

Norman (2006). Unfortunately, the observational constraints are scarce at high redshift, where simple extrapolations may not be valid. This is problematic for gravitational-wave sources, which preferentially form from low-metallicity star formation, which is most poorly constrained, especially at high redshift (see Chruślińska et al. 2021). We have therefore opted instead to make use of current state-of-the-art cosmological simulations (see also Briel et al. 2021, for a discussion). These provide physically motivated predictions at high redshift and have by now been extensively compared with observational constraints at lower redshift. Despite the large remaining uncertainties in these simulations, we believe this to be our best option at the current time.

Appendix D
The Redshift Dependence of the Merger Rate as a Function of Chirp Mass

In Figure 12, we show the same evolution of $R_{\rm BBH}(z)$ per primary BH mass, in the merger redshift—$M_{\rm BH,1}$ plane as displayed in Figure 3, but as a function of chirp mass, $M_{\rm chirp}$. We observe similar trends in the BBH merger distribution when we investigate $M_{\rm chirp}$ instead of $M_{\rm BH,1}$. Specifically, BBH mergers with high chirp mass ($M_{\rm chirp} > 20\,M_\odot$) originate predominantly from the stable RLOF channel, while the CE channel dominates the BBH merger rate for low chirp mass ($M_{\rm chirp} \leqslant 20\,M_\odot$).

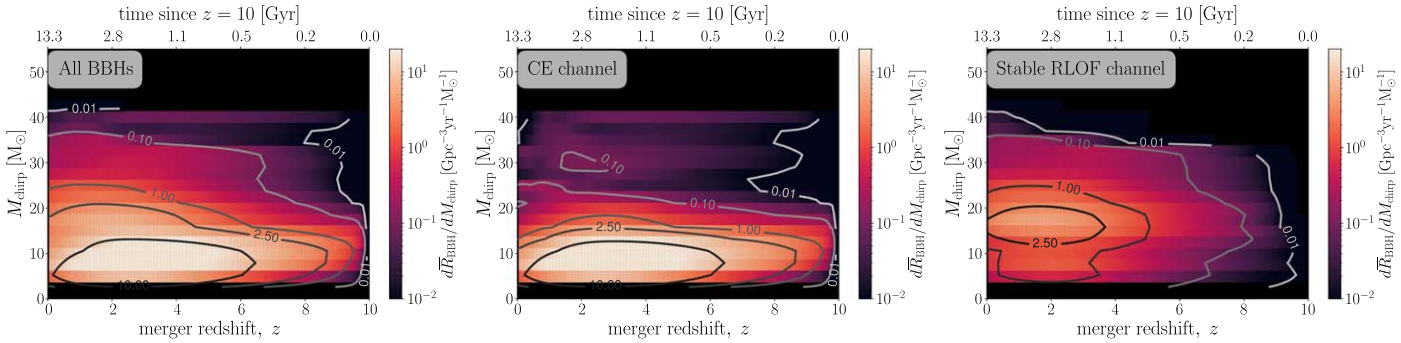

Figure 12. The averaged intrinsic merger rate density $\overline{R}_{\rm BBH}(z)$, for redshift bins of $dz = 0.2$ and chirp mass bins of $dM_{\rm chirp} = 2.5\,M_\odot$. The colors and symbols are the same as in Figure 3.

Appendix E
Mass Distribution Split by Formation Channel and Metallicity

In Figure 13, we show the $M_{\rm BH,1}$ distribution split by both formation channel and formation metallicity. We apply the same metallicity bins as those in Figure 7, but exclude the highest-metallicity bin in order to focus on metallicities low enough to form BHs with masses above $20\,M_\odot$. This shows that the stable RLOF channel dominates the high-mass end of the distribution at every metallicity.

Appendix F
Physics Variations

To test the robustness of our finding that the CE channel and stable RLOF channel lead to distinct distributions in delay time and primary BH mass, we use the grid of models presented in Broekgaarden et al. (2021a) and Broekgaarden et al. (2021b). These simulations were performed with a version of COMPAS that predates the publicly available code (most similar to version 02.13.01 of the publicly available code).

In Figures 14, 15, and 16, we show the distribution of primary BH mass ($M_{\rm BH,1}$) and delay time ($t_{\rm delay}$) similarly to Figure 2.

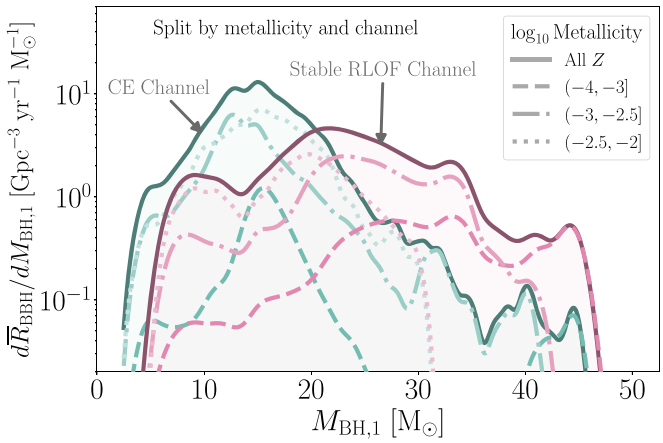

Figure 13. Distribution of primary BH masses $M_{\rm BH,1}$ split by formation channel and birth metallicity, for merger redshifts between $0 \leqslant z < 0.5$.

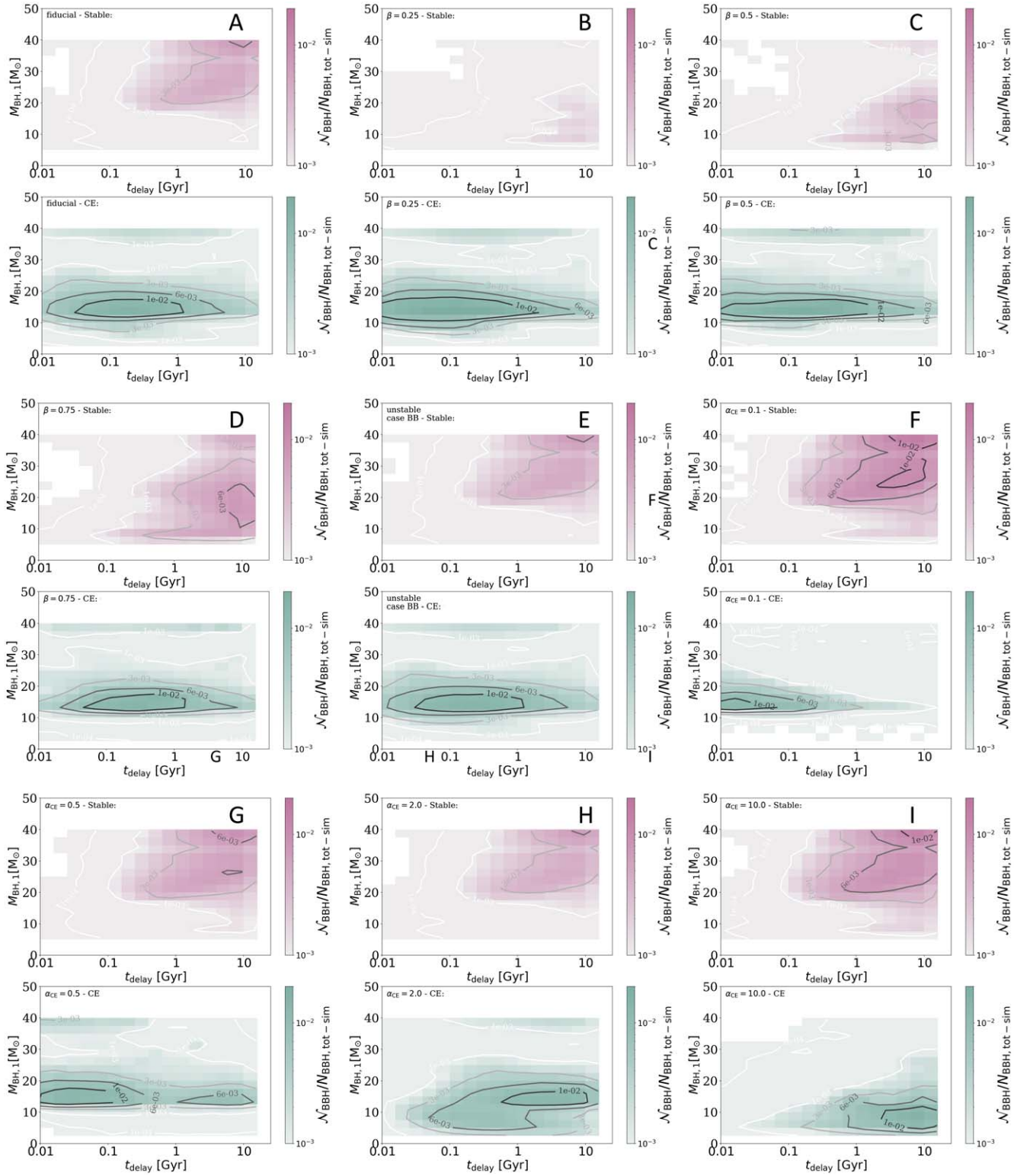

Figure 14. Same as Figure 2, but for several variations in the assumed model physics, based on models presented in Broekgaarden et al. (2021a) and Broekgaarden et al. (2021b). The models in each panel are as follows. Panel A: the fiducial model (see text). Panels B, C, and D: fixed mass-transfer efficiencies of $\beta = 0.25$, 0.5, and 0.75, respectively. Panel E: case BB mass transfer is assumed to always be unstable. Panels F, G, H, I: the CE efficiency parameter, $\alpha_{\rm CE}$, is set to respective values of 0.1, 0.5, 2.0, and 10.0.

Each panel in these figures displays a separate simulation of 53×10^6 binaries. The fiducial model in this grid (panel A in Figure 14) adopts physics assumptions that are very similar to our model assumptions as described in Section 2. The exceptions are the PPISN prescription (which follows Marchant et al. 2019), the metallicity sampling (which uses a discrete grid of 53 metallicities between 10^{-4}–0.03), and the LBV wind prescription (LBV-type stars, that is, stars above the Humphreys–Davidson limit, are assumed to receive an *additional* wind mass loss of $10^{-4}\,{\rm M}_\odot\,{\rm yr}^{-1}$, inspired by Belczynski et al. 2010).

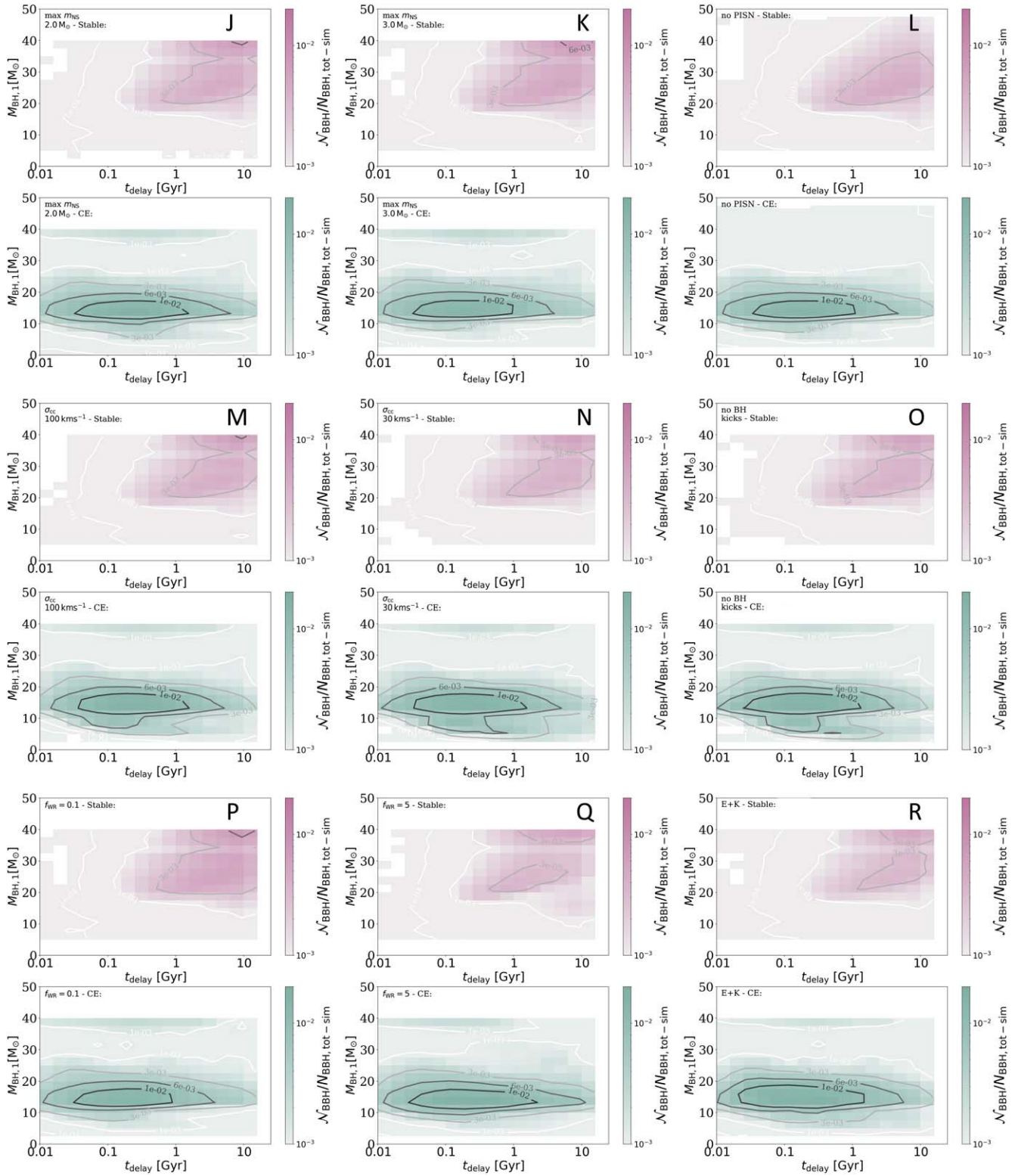

Figure 15. Same as Figure 14, but for the following model variations: Panels J and K: maximum neutron star mass is fixed to 2.0 $M_\odot$ and 3.0 $M_\odot$, respectively. Panel L: no PPISN or PISN implemented. Panels M and N: natal kicks are drawn from Maxwellian velocity distributions with respective one-dimensional root-mean-square velocity dispersions of $\sigma_{CC} = 100$ km s^{-1} and 30 km s^{-1}. Panel O: BHs are assumed to receive no natal kick. Panels P and Q vary the strength of the Wolf–Rayet-like wind mass loss by respective constant factors of $f_{WR} = 0.1$ and 5. Panel R combines the assumption that case BB mass transfer is always unstable with allowing Hertzsprung-gap donor stars that initiate a CE to survive the CE event (models E and S).

Each panel in Figures 14, 15, and 16 considers a physics variation with respect to the fiducial model in panel A. The variations are summarized in the caption of each figure, and for a full description of the physics assumptions, we direct the reader to Broekgaarden et al. (2021a) and Broekgaarden et al. (2021b).

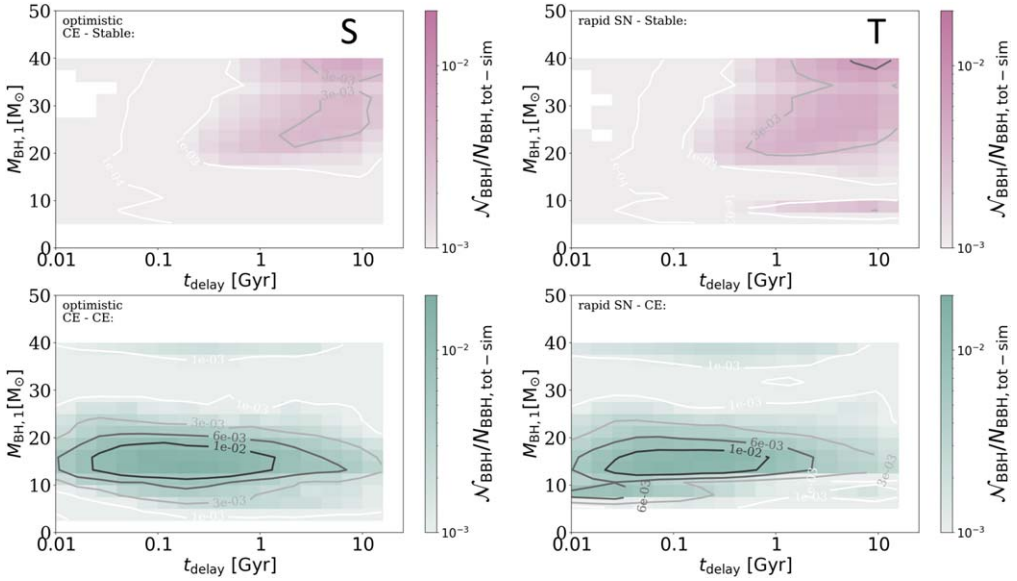

Figure 16. Same as Figure 14, but for the following model variations: Panel S: Hertzsprung-gap donor stars initiating a CE are allowed to survive this CE event. Panel T: adopts the Fryer et al. (2012) "rapid" supernova remnant-mass prescription.

Figures 14, 15, and 16 show that the dearth of BBH systems with high mass ($M_{\rm BH,1} > 30\,M_\odot$) and short delay time ($t_{\rm delay} \lesssim 1$ Gyr) is quite robust over numerous physics variations. Moreover, as discussed in Section 7, we retrieve distinct BH-mass and delay-time distributions for the two channels in almost all variations. The exceptions are the models that assume respective fixed values for the accretion efficiency β of 0.25 and 0.5 for episodes of mass transfer with a noncompact accretor (panels B and C in Figure 14), and the models that assume high values for the CE "efficiency parameter" ($\alpha_{\rm CE} = 2$ and $\alpha_{\rm CE} = 10$; panels H and I in Figure 14). Those variations in the accretion efficiency β diminish the contribution of the stable RLOF channel, and specifically reduce the production of high-mass $M_{\rm BH,1}$. This removes the distinction between the channels in the $M_{\rm BH,1}$ distribution. Assuming $\alpha_{\rm CE} = 10$ causes all the short delay-time systems from the CE channel to disappear. This is because, at higher $\alpha_{\rm CE}$, a BH needs to inspiral less deeply into its companion's envelope to achieve envelope ejection. This results in wider post-CE separations and hence more similar delay-time distributions for the two channels.

ORCID iDs

L. A. C. van Son https://orcid.org/0000-0001-5484-4987
S. E. de Mink https://orcid.org/0000-0001-9336-2825
T. Callister https://orcid.org/0000-0001-9892-177X
S. Justham https://orcid.org/0000-0001-7969-1569
M. Renzo https://orcid.org/0000-0002-6718-9472
T. Wagg https://orcid.org/0000-0001-6147-5761
F. S. Broekgaarden https://orcid.org/0000-0002-4421-4962
F. Kummer https://orcid.org/0000-0002-6056-3070
R. Pakmor https://orcid.org/0000-0003-3308-2420
I. Mandel https://orcid.org/0000-0002-6134-8946

References

Abbott, B. P., Abbott, R., Abbott, T. D., et al. 2017, CQGra, 34, 044001
Abbott, B. P., Abbott, R., Abbott, T. D., et al. 2018, LRR, 21, 3
Abbott, B. P., Abbott, R., Abbott, T. D., et al. 2019a, PhRvX, 9, 031040
Abbott, B. P., Abbott, R., Abbott, T. D., et al. 2019b, ApJ, 882, L24
Abbott, R., Abbott, T. D., Acernese, F., et al. 2021a, arXiv:2111.03606
Abbott, R., Abbott, T. D., Acernese, F., et al. 2021b, arXiv:2111.03634
Abbott, R., Abe, H., Acernese, F., et al. 2021c, arXiv:2111.03604
Abbott, R., Abbott, T. D., Abraham, S., et al. 2021d, ApJL, 913, L7
Abbott, R., Abbott, T. D., Abraham, S., et al. 2021e, ApJL, 913, L7
Abbott, T. D., Acernese, F., Ackley, K., et al. 2021f, arXiv:2108.01045
Abbott, R., Abbott, T. D., Abraham, S., et al. 2021g, PhRvX, 11, 021053
Ablimit, I., & Maeda, K. 2018, ApJ, 866, 151
Acernese, F., Agathos, M., Agatsuma, K., et al. 2015, CQGra, 32, 024001
Adams, S. M., Kochanek, C. S., Gerke, J. R., Stanek, K. Z., & Dai, X. 2017, MNRAS, 468, 4968
Adhikari, R. X., Arai, K., Brooks, A. F., et al. 2020, CQGra, 37, 165003
Akutsu, T., Ando, M., Arai, K., et al. 2021, PTEP, 2021, 05A101
Antonini, F., Chatterjee, S., Rodriguez, C. L., et al. 2016, ApJ, 816, 65
Antonini, F., Gieles, M., & Gualandris, A. 2019, MNRAS, 486, 5008
Antonini, F., Toonen, S., & Hamers, A. S. 2017, ApJ, 841, 77
Arca Sedda, M. 2020a, ApJ, 891, 47
Arca Sedda, M., Mapelli, M., Spera, M., Benacquista, M., & Giacobbo, N. 2020b, ApJ, 894, 133
Askar, A., Szkudlarek, M., Gondek-Rosińska, D., Giersz, M., & Bulik, T. 2017, MNRAS, 464, L36
Asplund, M., Grevesse, N., Sauval, A. J., & Scott, P. 2009, ARA&A, 47, 481
Astropy Collaboration, Price-Whelan, A. M., Sipőcz, B. M., et al. 2018, AJ, 156, 123
Astropy Collaboration, Robitaille, T. P., Tollerud, E. J., et al. 2013, A&A, 558, A33
Bae, Y.-B., Kim, C., & Lee, H. M. 2014, MNRAS, 440, 2714
Bardeen, J. M. 1970, Natur, 226, 64
Baruteau, C., Cuadra, J., & Lin, D. N. C. 2011, ApJ, 726, 28
Bavera, S. S., Fragos, T., Qin, Y., et al. 2020, A&A, 635, A97
Bavera, S. S., Fragos, T., Zevin, M., et al. 2021, A&A, 647, A153
Belczynski, K., Bulik, T., Fryer, C. L., et al. 2010, ApJ, 714, 1217
Belczynski, K., Bulik, T., & Rudak, B. 2004, ApJL, 608, L45
Belczynski, K., Dominik, M., Bulik, T., et al. 2010, ApJ, 715, L138
Belczynski, K., Holz, D. E., Bulik, T., & O'Shaughnessy, R. 2016, Natur, 534, 512
Belczynski, K., Repetto, S., Holz, D. E., et al. 2016, ApJ, 819, 108
Belczynski, K., Romagnolo, A., Olejak, A., et al. 2022, ApJ, 925, 69
Belczynski, K., Taam, R. E., Kalogera, V., Rasio, F. A., & Bulik, T. 2007, ApJ, 662, 504
Bellovary, J. M., Mac Low, M.-M., McKernan, B., & Ford, K. E. S. 2016, ApJL, 819, L17
Bouffanais, Y., Mapelli, M., Gerosa, D., et al. 2019, ApJ, 886, 25
Briel, M. M., Eldridge, J. J., Stanway, E. R., Stevance, H. F., & Chrimes, A. A. 2021, MNRAS, in press
Broekgaarden, F. S., Berger, E., Neijssel, C. J., et al. 2021a, MNRAS, 508, 5028

Broekgaarden, F. S., Berger, E., Stevenson, S., et al. 2021b, arXiv:2112.05763
Broekgaarden, F. S., Justham, S., de Mink, S. E., et al. 2019, MNRAS, 490, 5228
Brott, I., de Mink, S. E., Cantiello, M., et al. 2011, A&A, 530, A115
Callister, T., Fishbach, M., Holz, D. E., & Farr, W. M. 2020, ApJL, 896, L32
Callister, T. A., Haster, C.-J., Ng, K. K. Y., Vitale, S., & Farr, W. M. 2021, ApJL, 922, L5
Choksi, N., Volonteri, M., Colpi, M., Gnedin, O. Y., & Li, H. 2019, ApJ, 873, 100
Chruślińska, M., Belczynski, K., Klencki, J., & Benacquista, M. 2018, MNRAS, 474, 2937
Chruślińska, M., & Nelemans, G. 2019, MNRAS, 488, 5300
Chruślińska, M., Nelemans, G., & Belczynski, K. 2019, MNRAS, 482, 5012
Chruślińska, M., Nelemans, G., Boco, L., & Lapi, A. 2021, MNRAS, 508, 4994
Collette, A. 2013, h5py/h5py:v2.10.0, Zenodo
Costa, G., Bressan, A., Mapelli, M., et al. 2021, MNRAS, 501, 4514
Davies, B., & Beasor, E. R. 2020, MNRAS, 493, 468
Davies, B., Crowther, P. A., & Beasor, E. R. 2018, MNRAS, 478, 3138
de Kool, M. 1990, ApJ, 358, 189
de Mink, S. E., & Belczynski, K. 2015, ApJ, 814, 58
de Mink, S. E., Pols, O. R., Langer, N., & Izzard, R. G. 2009, A&A, 507, L1
Di Carlo, U. N., Giacobbo, N., Mapelli, M., et al. 2019, MNRAS, 487, 2947
Di Carlo, U. N., Mapelli, M., Bouffanais, Y., et al. 2020, MNRAS, 497, 1043
Dominik, M., Belczynski, K., Fryer, C., et al. 2012, ApJ, 759, 52
Dominik, M., Belczynski, K., Fryer, C., et al. 2013, ApJ, 779, 72
Dominik, M., Berti, E., O'Shaughnessy, R., et al. 2015, ApJ, 806, 263
Downing, J. M. B., Benacquista, M. J., Giersz, M., & Spurzem, R. 2010, MNRAS, 407, 1946
du Buisson, L., Marchant, P., Podsiadlowski, P., et al. 2020, MNRAS, 499, 5941
Eggleton, P. P. 1983, ApJ, 268, 368
Eldridge, J. J., & Stanway, E. R. 2016, MNRAS, 462, 3302
Farmer, R., Renzo, M., de Mink, S. E., Fishbach, M., & Justham, S. 2020, ApJL, 902, L36
Farmer, R., Renzo, M., de Mink, S. E., Marchant, P., & Justham, S. 2019, ApJ, 887, 53
Fernández, R., Quataert, E., Kashiyama, K., & Coughlin, E. R. 2018, MNRAS, 476, 2366
Fishbach, M., Doctor, Z., Callister, T., et al. 2021, ApJ, 912, 98
Fishbach, M., Holz, D. E., & Farr, W. M. 2018, ApJL, 863, L41
Fishbach, M., & Kalogera, V. 2021, ApJL, 914, L30
Fragione, G., & Banerjee, S. 2021, ApJL, 913, L29
Fragione, G., & Kocsis, B. 2018, PhRvL, 121, 161103
Fragione, G., & Silk, J. 2020, MNRAS, 498, 4591
Fryer, C. L., Belczynski, K., Wiktorowicz, G., et al. 2012, ApJ, 749, 91
Fuller, J., Cantiello, M., Lecoanet, D., & Quataert, E. 2015, ApJ, 810, 101
Gallegos-Garcia, M., Berry, C. P. L., Marchant, P., & Kalogera, V. 2021, ApJ, 922, 110
Ge, H., Webbink, R. F., Chen, X., & Han, Z. 2015, ApJ, 812, 40
Geha, M., Brown, T. M., Tumlinson, J., et al. 2013, ApJ, 771, 29
Genel, S., Nelson, D., Pillepich, A., et al. 2018, MNRAS, 474, 3976
Gennaro, M., Tchernyshyov, K., Brown, T. M., et al. 2018, ApJ, 855, 20
Giacobbo, N., & Mapelli, M. 2018, MNRAS, 480, 2011
Gilkis, A., Shenar, T., Ramachandran, V., et al. 2021, MNRAS, 503, 1884
Hamann, W.-R., & Koesterke, L. 1998, A&A, 335, 1003
Harris, C. R., Millman, K. J., van der Walt, S. J., et al. 2020, Natur, 585, 357
Hemler, Z. S., Torrey, P., Qi, J., et al. 2021, MNRAS, 506, 3024
Higgins, E. R., & Vink, J. S. 2020, A&A, 635, A175
Hild, S., Abernathy, M., Acernese, F., et al. 2011, CQGra, 28, 094013
Hinshaw, G., Larson, D., Komatsu, E., et al. 2013, ApJS, 208, 19
Hjellming, M. S., & Webbink, R. F. 1987, ApJ, 318, 794
Hoang, B.-M., Naoz, S., Kocsis, B., Rasio, F. A., & Dosopoulou, F. 2018, ApJ, 856, 140
Hobbs, G., Lorimer, D. R., Lyne, A. G., & Kramer, M. 2005, MNRAS, 360, 974
Hotokezaka, K., & Piran, T. 2017, ApJ, 842, 111
Humphreys, R. M., & Davidson, K. 1979, ApJ, 232, 409
Hunter, J. D. 2007, CSE, 9, 90
Hurley, J. R., Pols, O. R., & Tout, C. A. 2000, MNRAS, 315, 543
Hurley, J. R., Tout, C. A., & Pols, O. R. 2002, MNRAS, 329, 897
Inayoshi, K., Hirai, R., Kinugawa, T., & Hotokezaka, K. 2017, MNRAS, 468, 5020
Ivanov, M., & Fernández, R. 2021, ApJ, 911, 6
Ivanova, N., Justham, S., Chen, X., et al. 2013, A&ARv, 21, 59
Ivanova, N., Justham, S., & Ricker, P. 2020, Common Envelope Evolution (Bristol: IOP Publishing), 2514
Jiang, Y.-F., Cantiello, M., Bildsten, L., Quataert, E., & Blaes, O. 2015, ApJ, 813, 74
Jiang, Y.-F., Cantiello, M., Bildsten, L., et al. 2018, Natur, 561, 498
Kalari, V. M., Vink, J. S., Dufton, P. L., & Fraser, M. 2018, A&A, 618, A17
Kimpson, T. O., Spera, M., Mapelli, M., & Ziosi, B. M. 2016, MNRAS, 463, 2443
Kinugawa, T., Inayoshi, K., Hotokezaka, K., Nakauchi, D., & Nakamura, T. 2014, MNRAS, 442, 2963
Klencki, J., Nelemans, G., Istrate, A. G., & Chruślińska, M. 2021, A&A, 645, A54
Kluyver, T., Ragan-Kelley, B., Pérez, F., et al. 2016, in Positioning and Power in Academic Publishing: Players, Agents and Agendas, ed. F. Lozides & B. chmidt (Amsterdam: IOS Press), 87
Kremer, K., Spera, M., Becker, D., et al. 2020, ApJ, 903, 45
Kroupa, P. 2001, MNRAS, 322, 231
Kudritzki, R. P., Pauldrach, A., Puls, J., & Abbott, D. C. 1989, A&A, 219, 205
Kudritzki, R. P., & Reimers, D. 1978, A&A, 70, 227
Kummer, F. 2020, MSc Thesis, University of Amsterdam
Kushnir, D., Zaldarriaga, M., Kollmeier, J. A., & Waldman, R. 2016, MNRAS, 462, 844
Langer, N., & Norman, C. A. 2006, ApJL, 638, L63
Leigh, N. W. C., Geller, A. M., McKernan, B., et al. 2018, MNRAS, 474, 5672
LIGO Scientific Collaboration, Aasi, J., Abbott, B. P., et al. 2015, CQGra, 32, 074001
Lovegrove, E., & Woosley, S. E. 2013, ApJ, 769, 109
Madau, P., & Dickinson, M. 2014, ARA&A, 52, 415
Maggiore, M., Van Den Broeck, C., Bartolo, N., et al. 2020, JCAP, 2020, 050
Mandel, I., & Broekgaarden, F. S. 2022, LRR, 25, 1
Mandel, I., & de Mink, S. E. 2016, MNRAS, 458, 2634
Mandel, I., & Farmer, A. 2022, PhR, 955, 1
Mandel, I., Farr, W. M., & Gair, J. R. 2019, MNRAS, 486, 1086
Mandel, I., & Fragos, T. 2020, ApJL, 895, L28
Mapelli, M. 2021, in Handbook of Gravitational Wave Astronomy, ed. C. Bambi et al. (Berlin: Springer), 4
Mapelli, M., Bouffanais, Y., Santoliquido, F., Arca Sedda, M., & Artale, M. C. 2022, MNRAS, 511, 5797
Mapelli, M., & Giacobbo, N. 2018, MNRAS, 479, 4391
Mapelli, M., Giacobbo, N., Ripamonti, E., & Spera, M. 2017, MNRAS, 472, 2422
Mapelli, M., Giacobbo, N., Santoliquido, F., & Artale, M. C. 2019, MNRAS, 487, 2
Mapelli, M., Zampieri, L., Ripamonti, E., & Bressan, A. 2013, MNRAS, 429, 2298
Marchant, P., Langer, N., Podsiadlowski, P., Tauris, T., & Moriya, T. 2016, A&A, 588, A50
Marchant, P., & Moriya, T. J. 2020, A&A, 640, L18
Marchant, P., Pappas, K. M. W., Gallegos-Garcia, M., et al. 2021, A&A, 650, A107
Marchant, P., Renzo, M., Farmer, R., et al. 2019, ApJ, 882, 36
Marigo, P., Girardi, L., Chiosi, C., & Wood, P. R. 2001, A&A, 371, 152
Marinacci, F., Vogelsberger, M., Pakmor, R., et al. 2018, MNRAS, 480, 5113
Martín-Navarro, I., La Barbera, F., Vazdekis, A., Falcón-Barroso, J., & Ferreras, I. 2015, MNRAS, 447, 1033
McKernan, B., Ford, K. E. S., & O'Shaughnessy, R. 2020, MNRAS, 498, 4088
Mehta, A. K., Buonanno, A., Gair, J., et al. 2022, ApJ, 924, 39
Mennekens, N., & Vanbeveren, D. 2014, A&A, 564, A134
Miller, S., Callister, T. A., & Farr, W. M. 2020, ApJ, 895, 128
Nadezhin, D. K. 1980, Ap&SS, 69, 115
Naiman, J. P., Pillepich, A., Springel, V., et al. 2018, MNRAS, 477, 1206
Nebot Gómez-Morán, A., Gänsicke, B. T., Schreiber, M. R., et al. 2011, A&A, 536, A43
Neijssel, C. J., Vigna-Gómez, A., Stevenson, S., et al. 2019, MNRAS, 924, 2457
Nelson, D., Pillepich, A., Springel, V., et al. 2018, MNRAS, 475, 624
Neo, S., Miyaji, S., Nomoto, K., & Sugimoto, D. 1977, PASJ, 29, 249
Ng, K. K. Y., Vitale, S., Farr, W. M., & Rodriguez, C. L. 2021, ApJL, 913, L5
Nieuwenhuijzen, H., & de Jager, C. 1990, A&A, 231, 134
O'Hagan, A., & Leonard, T. 1976, Biometrika, 63, 201
Olejak, A., & Belczynski, K. 2021, ApJL, 921, L2
Olejak, A., Belczynski, K., & Ivanova, N. 2021, A&A, 651, A100
Öpik, E. 1924, Tartu Obs. Publ, 25, 6
Paczynski, B. 1976, IAUS, 73, 75
Pakmor, R., Springel, V., Bauer, A., et al. 2016, MNRAS, 455, 1134
Pavlovskii, K., & Ivanova, N. 2015, MNRAS, 449, 4415

Pavlovskii, K., Ivanova, N., Belczynski, K., & Van, K. X. 2017, MNRAS, 465, 2092
Paxton, B., Marchant, P., Schwab, J., et al. 2015, ApJS, 220, 15
Perez, F., & Granger, B. E. 2007, CSE, 9, 21
Peters, P. C. 1964, PhRv, 136, 1224
Petrovich, C., & Antonini, F. 2017, ApJ, 846, 146
Pillepich, A., Nelson, D., Hernquist, L., et al. 2018a, MNRAS, 475, 648
Pillepich, A., Springel, V., Nelson, D., et al. 2018b, MNRAS, 473, 4077
Pols, O. R., Schröder, K.-P., Hurley, J. R., Tout, C. A., & Eggleton, P. P. 1998, MNRAS, 298, 525
Pols, O. R., Tout, C. A., Schröder, K.-P., Eggleton, P. P., & Manners, J. 1997, MNRAS, 289, 869
Portegies Zwart, S. F., & McMillan, S. L. W. 2000, ApJL, 528, L17
Postnov, K. A., & Yungelson, L. R. 2014, LRR, 17, 3
Punturo, M., Abernathy, M., Acernese, F., et al. 2010, CQGra, 27, 084007
Rebassa-Mansergas, A., Gänsicke, B. T., Rodríguez-Gil, P., Schreiber, M. R., & Koester, D. 2007, MNRAS, 382, 1377
Rebassa-Mansergas, A., Nebot Gómez-Morán, A., Schreiber, M. R., et al. 2012, MNRAS, 419, 806
Reitze, D., Adhikari, R. X., Ballmer, S., et al. 2019, BAAS, 51, 35
Renzo, M., Farmer, R., Justham, S., et al. 2020a, A&A, 640, A56
Renzo, M., Farmer, R. J., Justham, S., et al. 2020b, MNRAS, 493, 4333
Riley, J., Agrawal, P., Barrett, J. W., et al. 2022, ApJS, 258, 34
Riley, J., Mandel, I., Marchant, P., et al. 2021, MNRAS, 505, 663
Rodriguez, C. L., & Antonini, F. 2018, ApJ, 863, 7
Rodriguez, C. L., & Loeb, A. 2018, ApJL, 866, L5
Rodriguez, C. L., Zevin, M., Amaro-Seoane, P., et al. 2019, PhRvD, 100, 043027
Roulet, J., & Zaldarriaga, M. 2019, MNRAS, 484, 4216
Sabhahit, G. N., Vink, J. S., Higgins, E. R., & Sander, A. A. C. 2021, MNRAS, 506, 4473
Sana, H., de Mink, S. E., de Koter, A., et al. 2012, Sci, 337, 444
Santoliquido, F., Mapelli, M., Giacobbo, N., Bouffanais, Y., & Artale, M. C. 2021, MNRAS, 502, 4877
Sanyal, D., Grassitelli, L., Langer, N., & Bestenlehner, J. M. 2015, A&A, 580, A20
Sanyal, D., Langer, N., Szécsi, D., -C Yoon, S., & Grassitelli, L. 2017, A&A, 597, A71
Sathyaprakash, B., Bailes, M., Kasliwal, M. M., et al. 2019b, BAAS, 51, 276
Sathyaprakash, B., Belgacem, E., Bertacca, D., et al. 2019a, BAAS, 51, 248
Schneider, F. R. N., Sana, H., Evans, C. J., et al. 2018, Sci, 361, aat7032
Secunda, A., Bellovary, J., Mac Low, M.-M., et al. 2019, ApJ, 878, 85
Shao, Y., & Li, X.-D. 2021, arXiv:2107.03565
Smith, N. 2014, ARA&A, 52, 487
Soberman, G. E., Phinney, E. S., & van den Heuvel, E. P. J. 1997, A&A, 327, 620
Song, H. F., Maeder, A., Meynet, G., et al. 2013, A&A, 556, A100
Song, H. F., Meynet, G., Maeder, A., Ekstrom, S., & Eggenberger, P. 2016, A&A, 585, A120
Spera, M., Mapelli, M., Giacobbo, N., et al. 2019, MNRAS, 485, 889
Springel, V. 2010, MNRAS, 401, 791
Springel, V., Pakmor, R., Pillepich, A., et al. 2018, MNRAS, 475, 676
Steinle, N., & Kesden, M. 2021, PhRvD, 103, 063032
Stevenson, S., Berry, C. P. L., & Mandel, I. 2017, MNRAS, 471, 2801
Stevenson, S., Vigna-Gómez, A., Mandel, I., et al. 2017, NatCo, 8, 14906
Talbot, C., & Thrane, E. 2018, ApJ, 856, 173
Tchekhovskoy, A., McKinney, J. C., & Narayan, R. 2012, JPhCS, 372, 012040
Torrey, P., Vogelsberger, M., Marinacci, F., et al. 2019, MNRAS, 484, 5587
van den Heuvel, E. P. J., Portegies Zwart, S. F., & de Mink, S. E. 2017, MNRAS, 471, 4256
van Rossum, G. 1995, Python 3 Reference Manual (Scotts Valley, CA: CreateSpace)
van Son, L. A. C., De Mink, S. E., Broekgaarden, F. S., et al. 2020, ApJ, 897, 100
Vassiliadis, E., & Wood, P. R. 1993, ApJ, 413, 641
Vigna-Gómez, A., MacLeod, M., Neijssel, C. J., et al. 2020, PASA, 37, e038
Vigna-Gómez, A., Neijssel, C. J., Stevenson, S., et al. 2018, MNRAS, 481, 4009
Vink, J. S., & de Koter, A. 2005, A&A, 442, 587
Vink, J. S., de Koter, A., & Lamers, H. J. G. L. M. 2000, A&A, 362, 295
Vink, J. S., de Koter, A., & Lamers, H. J. G. L. M. 2001, A&A, 369, 574
Virtanen, P., Gommers, R., Oliphant, T. E., et al. 2020, NatMe, 17, 261
Vitale, S., Farr, W. M., Ng, K. K. Y., & Rodriguez, C. L. 2019, ApJL, 886, L1
Waskom, M. L. 2021, JOSS, 6, 3021
Webbink, R. F. 1984, ApJ, 277, 355
Weinberger, R., Springel, V., & Pakmor, R. 2020, ApJS, 248, 32
Wong, K. W. K., Breivik, K., Kremer, K., & Callister, T. 2021, PhRvD, 103, 083021
Woosley, S. E., & Heger, A. 2021, ApJL, 912, L31
Xu, X.-J., & Li, X.-D. 2010a, ApJ, 716, 114
Xu, X.-J., & Li, X.-D. 2010b, ApJ, 722, 1985
Yang, Y., Bartos, I., Gayathri, V., et al. 2019, PhRvL, 123, 181101
Zaldarriaga, M., Kushnir, D., & Kollmeier, J. A. 2018, MNRAS, 473, 4174
Zevin, M., Bavera, S. S., Berry, C. P. L., et al. 2021, ApJ, 910, 152
Ziosi, B. M., Mapelli, M., Branchesi, M., & Tormen, G. 2014, MNRAS, 441, 3703